Abstract

Fragmentation is a phenomenon which appears at all time and length scales in nature. Hence, it has a profound impact on many interesting physical and biological systems. *Brittle* fragmentation is free from effects due to plasticity and viscoelasticity and so serves as a test bench for understanding the fundamental mechanisms in fragmentation.

The aim of the present work is to investigate the inherent mechanisms of dynamic brittle fragmentation in different spatial dimensions. To this end, we introduce conceptual models of dynamic fragmentation. We also introduce two coarse-grained numerical models for generic brittle materials, which are dynamically realistic. The first numerical model describes fragmentation of D-dimensional objects in D-dimensional space for $D = 2$. In the model a two dimensional object under fragmentation is embedded in two dimensional space. The second numerical model is fully periodic (a torus), and describes fragmentation of a two dimensional object in three-dimensional space.

For the case when the spatial dimension equals that of the fragmenting object, an analytical model based on branching and merging of propagating cracks is introduced. Merging of side branches results in a scale-invariant fragment-size distribution with a universal scaling exponent $(2D - 1)/D$. The model is verified both numerically and experimentally. The experimental fragment-size distributions are given with excellent accuracy by the analytical model over several orders of magnitude in the small damping limit. Correlation length exponent is however shown to be non-universal and depend upon material and loading conditions.

With the second numerical model we show that the extra spatial dimension allows an additional (hierarchical) fragmentation mechanism on top of those related to mergers of uncorrelated cracks on the one hand and of their side branches on the other hand. Hierarchical mechanism also results in a scale invariant fragment-size distribution but with a different scaling exponent. This mechanism explains some experimental results which have previously been unexplained.

i

Preface

The work included in this thesis was done during 2001-2004 in the Department of Physics at the University of Jyväskylä. I thank my supervisor Prof. Jussi Timonen for giving me a fair chance to do it and for his valuable contribution in the final stages of processing the manuscripts and the thesis. I also want to thank Prof. Risto Nieminen for kindly arranging so that I could perform the work in the Laboratory of Physics at HUT having its excellent facilities at my disposal.

To my instructor Dr. Jan Åström many thanks are in order. The problem with a new person introduced to a field where the group already has long traditions and established working relations is that most of the ideas he comes up with after hard work are to some extent already familiar to the senior members. Thus, a vast amount of work tends to go more or less unrecognised. The position is not particularly gratifying to the newcomer, but on the other hand teaches him the necessity of being able to develop the upcoming concepts into a presentable form. I think the period of making this thesis has taught me to collaborate, but on the other hand to work independently and have confidence in myself. For this lesson I am indebted to Jan. He has also been a good 'brother in harms' in the academic environment, where the bottom line to most human relations is 'you ain't never caught a rabbit, you ain't no friend of mine'.

My warmest thanks go to Tarja for her love and for encouraging me to have faith, when in tight spots. Also, it is hard to find proper words to thank the two witty kids, Ilona and Juhani, for their unconditional love and affection. When with them, I often realise that the apparently big problems and inventions are not so great after all.

Espoo, June 2004

Riku Linna

ii

Contents

List of Publications

This thesis consists of an overview and the following publications:

I R.P. Linna, J.A. Åström, and J. Timonen, "Unconstrained Periodic Boundary Conditions for Solid State Elasticity", Computer Physics Communications **158**, 26-38 (2004).

II J.A. Åström, R.P. Linna, J. Timonen, P.F. Møller, and L. Oddershede, "Exponential and Power-law Mass Distributions in Brittle Fragmentation", accepted for publication in Physical Review E.

III J.A. Åström, F. Ouchterlony, R.P. Linna, and J. Timonen, "Universal Dynamic Fragmentation in D Dimensions", Physical Review Letters **92**, 245506 (2004).

IV R.P. Linna, J.A. Åström, and J. Timonen, "Dimensional Effects in Dynamic Fragmentation of Brittle Materials", submitted to Physical Review Letters.

The author has had an active part in all stages of the research. He has been involved in planning and conducting the research. He has designed and written the simulation programs used in Publications I and IV. He has performed the initial numerical work leading to the reported work in Publications II and III. He has actively contributed to the ideas, concepts, and calculations in Publications II and III and written parts of them and performed some of the simulations reported in Publication III. He has done the analytic and numerical work reported in Publications I and IV and written Publication I and the first draft of Publication IV.

Chapter 1

Introduction

Fragmentation is a fundamental process that appears in many phenomena in nature. It takes place practically at all length and time scales ranging from those relevant in the breakup of heavy nuclei [1, 2], in polymer degradation [3], in mineral processing [4], up to the size distribution of asteroids [5]. In the case of *instantaneous* fracture, *i.e.* the one which results from sudden introduction of a sufficiently strong external energy that breaks the object into smaller fragments, the fragmentation process falls into three main regimes in the order of increasing applied energy [6]: abrasion, cleavage, and shattering. In abrasion only a small part from the surface of the object is fractured, shattering is destructive breaking, whereas cleavage is defined as a process in which the energy input just suffices for one crack to propagate through the sample. This classification is evidently highly dependent upon the geometry and the loading conditions of the sample. For instance, the concept of abrasion is meaningful only in the case when the sample is loaded at its boundaries.

As most of the experimental data available are on instantaneous fragmentation, many theoretical, computational and statistical models consider *continuous* fragmentation. In the terminology presented above, the greatest interest concerns the regime close to cleavage. As abrasion is a rather qualitative concept, we prefer to divide the process into two regimes that we call the *damaged* and the *fragmented* state of the system, as presented in [7]. When the rate of elastic energy fed into the system (*i.e.* strain rate) is smaller than a sample dependent value, the sample will be merely damaged, whereas at higher rates cracks will propagate through the sample and it becomes fragmented. At large enough strain rates the sample is destructed (*shattering*).

In many experiments of fragmentation, a power-law dependence in the fragment-size distribution (FSD) over a non-negligible range of fragment sizes has been obtained, (*e.g.* [4, 8, 9, 10, 11, 12, 13]). This has inspired numerous attempts to

explain the behaviour by computational and theoretical models. Most of the presented theoretical models are geometrical or probabilistic [14, 15, 16] and thus fail to take into account the dynamical aspects of the process. An important dynamical model revealing the potential criticality of impact fragmentation with respect to the imparted energy was reported in [7]. This study also suggested the potential importance of the dynamical aspects of fragmentation. The present study focuses on dynamics and on mechanisms of fragmentation responsible for the observed scale invariance in FSD. The existence of a transition point to the fragmented state in the imparted energy was rather satisfactorily shown already in [7, 17], and evident in all of our simulations, so that we study the systems close to this transition.

Another aspect that has escaped detailed analysis is the effect of related dimensions. Although clear experimental evidence [9, 10] of its importance has been available, no clear explanation to it has so far been attempted. The aim of this thesis is to identify the basic mechanisms in dynamical fragmentation and to extract effects related to the dimension of the fragmenting sample versus the spatial dimension.

The thesis can be outlined as follows. In Chapter 2 the concepts and models of fracture and fragmentation most relevant to the present study are presented. For the needs of lattice dynamics to be introduced later, some equations of motion are also derived in 2D, and a few relevant experimental results are reviewed.

The numerical methods and the models introduced in the thesis are presented in Chapter 3.

The main results are outlined in Chapter 4. An analytical branching-merging model is presented and verified by simulations and by comparison with experimental data. An extension of this model to fragmentation of 2D objects in 3D space with an additional hierarchical fragmentation mechanism is introduced and analysed, and verified by numerical simulations as well as by comparison with previous experimental results.

General conclusions based on the results obtained are drawn in Chapter 5.

Chapter 2

Fragmentation

2.1   Background

Compared to many other branches of physics, the development of our theoretical understanding of fragmentation has progressed slowly. This is largely due to the difficulty in obtaining experimental data that would shed more light into the inherent dynamics of large-scale fragmentation. Almost all models and theories thus aim at explaining features observed in the final distribution of the fragments. The size distributions of fragments that arise from instantaneous breaking serve as fundamental building blocks upon which theories for continuous breakup of materials can be constructed. There is a number of equivalent forms used for expressing the fragment size distribution [6]. In experiments the most commonly used form is the cumulative mass of fragments of linear dimension *less* than r, $M(r)$, naturally obtained in sieving measurements. This type of measurement also provides the cumulative number $N(s)$ of fragments with mass *greater* than a given mass s, $N(s)$. Many theoretical treatments, including the present one, often express the size distribution in terms of the number density of fragments with a mass between s and $s + ds$, $c(s)$, $n(s)$. It has been known for quite some while that, in the limit of small masses, these distributions are often well described by the equivalent power-law forms [18]

$$
\begin{aligned}
M(r) &\propto r^{3(2-\alpha)}, \\
N(s) &\propto s^{-(\alpha-1)}, \\
n(s) &\propto s^{-\alpha}.
\end{aligned}
\tag{2.1}
$$

In many experiments on instantaneous and highly energetic breaking, values between 5/3 and 11/6 have been quoted for exponent α [6]. In the references up to 1984, the

power-law form had been obtained over at most two orders of magnitude in size in the small size limit [8, 19, 20].

An early theoretical attempt worth mentioning was that by Kolmogorov [21]. He started by presenting a simple multiplicative argument for repeated fragmentation: The mass of a given fragment evolves as $s_0 \rightarrow s_1 \rightarrow \cdots \rightarrow s_N$, where the successive reduction factor, $r_k = s_k/s_{k-1}$, is a random variable with a well-behaved distribution. By the central limit theorem, $\log s_N = \sum_{k=0}^{N} \log r_k$ will be normally distributed, so that s_N will be distributed *log-normally*. The log-normal distribution described adequately the size distribution in some geological situations, such as the distribution of rock sizes in boulder fields and of particle sizes in soils [22, 23, 24, 25]. The argument contains the implicit assumption of fragmentation proceeding in discrete stages with each object undergoing approximately the same number of breakup events [6]. However, this does not seem an overly drastic assumption as the fragments do appear in a sense in a discrete fashion as a result of crack propagation.

In the following, we first outline in Sec. 2.2.1 the equilibrium arguments for crack propagation, which can be considered as a starting point for fracture research. We then derive some elastodynamic equations in 2D, which are relevant to crack dynamics. As fragmentation is based on the elastodynamic behaviour of the material undergoing fracture, we give a brief account of some relevant aspects of continuum theory in Sec. 2.2.2. Thereafter some experimental results for fracture dynamics, which have relevance to fragmentation, are reviewed in Sec. 2.2.3. We then outline some of the conceptual development in fragmentation and the related experimental results, relevant to the present study, in Secs. 2.3 and 2.4. As no well defined theory exists of either fracture dynamics or dynamical fragmentation, we only bring up a number of relevant concepts and observations based on experiments and simulations.

2.2 Fracture dynamics

2.2.1 Equilibrium theory

Fracture is distinctively a non-equilibrium process. Still, many of the first significant contributions to the field were made assuming equilibrium conditions. Among them, the work of Griffith is undoubtedly the most significant [26]. He considered an ideally brittle elastic body containing a crack and potential energy of the form $E_{pot} = \Omega + \Omega_S$, where the first term is the elastic energy of the sample and the second is the energy expended in forming new surface as the crack grows. If the work per unit area of surface created is denoted by γ, then for a crack to grow a length l, $\Omega_S = 2\gamma l$. Griffith then invoked the equilibrium principle of minimum potential energy for conservative systems by considering the system to be in equilibrium with

a particular fixed loading and a particular crack length. He then postulated that the crack was at the critical state of *incipient growth* if the reduction in macroscopic potential energy associated with a small virtual crack advance from that state was equal to the microscopic work of creating the corresponding crack surface area,

$$\frac{\partial}{\partial l}(\Omega + \Omega_S) = 0. \tag{2.2}$$

The state of incipient growth is an equilibrium state, and the crack length solved from Eq. (2.2), $l = l_c$, is called the critical length for incipient growth. However, the form of the elastic energy Ω as a function of l determines the nature of the system. Typically, for a constant displacement loading $\partial^2/\partial l^2(\Omega + \Omega_S) > 0$, and thus, under equilibrium conditions, the crack will advance slowly in increasing displacement. Thus in the above equation $-\partial\Omega/\partial l$ can be interpreted as a crack driving force. If, on the other hand, $\partial^2/\partial l^2(\Omega + \Omega_S) < 0$, as is typically the case for force-loaded systems, the system is unstable against crack growth and the crack will advance without further driving.

Mott proposed a theoretical framework for including inertial effects during the rapid crack growth [27] based on Griffith's analysis. He introduced the total kinetic energy for the system in the form $T_{tot} = v^2 f(l)$, where v is the velocity of the crack tip, and argued that the total energy of this system is constant,

$$\frac{\partial}{\partial l}(\Omega + T_{tot} + \Omega_S) = 0. \tag{2.3}$$

Although some wrong conclusions from this steady-state crack growth model were inferred, the basic idea of energy balance during rapid crack growth was important for the later progress in the field.

Important for the development of the continuum field approach to fracture was that Irwin introduced the concept of elastic stress intensity factor K [28]. He demonstrated the equivalence of his stress intensity factor criterion and the Griffith energy criterion for the onset of growth of a tensile crack in a two-dimensional plane under given stress, and showed that the energy release rate is given by

$$G = -\frac{\partial\Omega}{\partial l} = \frac{K^2}{E}, \tag{2.4}$$

where E is the Young's modulus of the material [29].

2.2.2 Dynamic theory

Irwin's introduction of stress intensity factor K provided the basis for the development of theoretical dynamic fracture mechanics. The dynamic fracture mechanics

is naturally based on continuum mechanics. In the basic solutions in the field the stress waves invoked by the propagating crack are accounted for in various approximative schemes. As the conceptual and numerical models presented in this work are mainly in 2D, it is in order to review here the basic continuum equations in 3D and to derive their 2D counterparts. Besides, the 3D versions are often used in 2D as well. The equation of motion for an elastic continuum is

$$\rho \ddot{u}_i = \partial \sigma_{ik} / \partial x_k, \tag{2.5}$$

where ρ is the mass density, u_i are the displacement vector, and σ_{ik} the stress tensor components and x_k the position coordinates ($i, k \in \{x, y, z\}$). The rhs of Eq. (2.5) is thus the internal stress force (summation over repeated index). The free energy of a deformed isotropic body can be expressed as

$$F = F_0 + \frac{1}{2} \lambda u_{ii}^2 + \mu u_{ik}^2, \tag{2.6}$$

where F_0 is the free energy of the undeformed body, and λ and μ are Lamé constants. To represent deformations as the sum of a pure shear and a hydrostatic compression, the following identity can be used:

$$u_{ik} = (u_{ik} - A\delta_{ik} u_{ll}) + A\delta_{ik} u_{ll}. \tag{2.7}$$

Here, $A = 1/3$ for 3D and $A = 1/2$ for 2D (as $\delta_{ii} = 1/A$). The differences in the relevant equations of motion in different spatial dimensions arise basically from this identity. Omitting the unnecessary F_0, since it can be chosen as the reference energy level, the free energy can now be expressed as

$$F = \mu(u_{ik} - A\delta_{ik} u_{ll})^2 + \frac{1}{2} \kappa u_{ll}^2, \tag{2.8}$$

where $\kappa = -V(\partial p / \partial V)_T$ is the modulus of compression, and

$$\begin{aligned}
\kappa &= \lambda + \frac{2}{3} \mu, && \text{in 3D}, \\
\kappa &= \lambda + \mu, && \text{in 2D}.
\end{aligned} \tag{2.9}$$

The stress tensor can be expressed as

$$\begin{aligned}
\sigma_{ik} &= K u_{ll} \delta_{ik} + 2\mu(u_{ik} - \frac{1}{3} \delta_{ik} u_{ll}), && \text{in 3D}, \\
\sigma_{ik} &= K u_{ll} \delta_{ik} + 2\mu(u_{ik} - \frac{1}{2} \delta_{ik} u_{ll}), && \text{in 2D}.
\end{aligned} \tag{2.10}$$

The coefficients in Eq. (2.8) may be expressed in terms of the Poisson ratio $\nu = -u_{ii}/u_{jj}$. Spatial dimension does not affect the coefficient of the shear term μ, but

does affect that of the compression term κ,

$$
\begin{aligned}
\mu &= \frac{E}{2(1+\nu)}, && \text{in 2D and 3D,} \\
\kappa &= \frac{E}{3(1-2\nu)}, && \text{in 3D,} \\
\kappa &= \frac{E}{2(1-\nu)}, && \text{in 2D.}
\end{aligned}
\tag{2.11}
$$

The equation of motion - or Navier's equation - can now be expressed as

$$
\begin{aligned}
\rho\ddot{\vec{u}} &= \frac{E}{2(1+\nu)}\triangle\vec{u} + \frac{E}{2(1+\nu)(1-2\nu)}\nabla\nabla\cdot\vec{u}, && \text{in 3D,} \\
\rho\ddot{\vec{u}} &= \frac{E}{2(1+\nu)}\triangle\vec{u} + \frac{E}{2(1-\nu)}\nabla\nabla\cdot\vec{u}, && \text{in 2D.}
\end{aligned}
\tag{2.12}
$$

The longitudinal (c_l)and transverse (c_t) elastic wave velocities can be deduced from these equations such that

$$
\begin{aligned}
c_l &= \sqrt{\frac{E(1-\nu)}{\rho(1+\nu)(1-2\nu)}}, \quad c_t = \sqrt{\frac{E}{2\rho(1+\nu)}}, && \text{in 3D,} \\
c_l &= \sqrt{\frac{E}{\rho(1+\nu)(1-\nu)}}, \quad c_t = \sqrt{\frac{E}{2\rho(1+\nu)}}, && \text{in 2D.}
\end{aligned}
\tag{2.13}
$$

The derivation given in [31] for the velocity of the surface wave c_R is valid in 2D as well. Only the ratio $c_t/c_l = \sqrt{(1-\nu)/2}$ differs from the 3D case. Due to this, the maximum value for the proportionality factor ξ in 2D,

$$
c_R = \xi c_t,
\tag{2.14}
$$

is less than that in 3D, $\xi_{3D} \approx 0.875$ [31].

All solutions to moving cracks in different geometries start from the Navier's equation, Eq. (2.5). Typically, in fracture mechanics solutions are sought for boundary value problems in plane geometries in which continuum materials are of infinite thickness, so 3D equations are used. These results should not be uncritically adopted as such to two-dimensional materials, but solutions should start from the 2D forms given above. The basic continuum mechanical constraints are imposed while solving the problem in addition to the conservation of linear momentum, which leads to Navier's equation, *i.e.* conservation of mass, $\dot{\rho} + \rho\partial_{x_i}\partial_t v_i = 0$, and the conservation of angular momentum that requires that the stress tensor is symmetric, $\sigma_{ij} = \sigma_{ji}$. The crack naturally introduces a discontinuity in the geometry. In the crack domain

conservation of linear momentum is replaced by $\|\sigma_{ij}n_i + \rho V \dot{u}_j\| = 0$, where notation $\|f\| = f^+ - f^-$ denotes the jump in the value of function f across the crack surface: its limiting values are $f^{\pm}$ as the surface is approached in the direction of $n_i^{\pm}$, with n_i the unit normal vectors of the crack surface. V is the local speed of the surface in the direction of the unit normal.

The boundary value problems are solved by applying techniques of complex integration. The crack tip is treated as a normal discontinuity. The discontinuity related to the opened crack surface presents extra complications, however. As part of the solution the speed for elastic waves travelling in opposite directions along the crack surfaces is obtained. This is the speed of free surface Rayleigh waves, c_R. Theoretically, c_R is the upper limit for the crack propagation speed.

Only in a few cases the boundary value problem can be solved exactly. Already for stationary crack growth the solutions become complicated, let alone for crack growth at a nonuniform speed. The basic elastodynamic solutions shed no light *e.g* into the important question of cracks turning towards each other and the angle at which they meet. The non-stationary boundary conditions of this problem make it inaccessible for analytic solutions. So, the best that has been done analytically so far has been to find solutions for a single crack propagating under various boundary conditions. The stress intensity factor varies with varying geometry and crack opening mode, but the asymptotic form of the stress field near the crack tip is always the same. In polar coordinates around the crack tip

$$\sigma_{ij} = \frac{K_\eta}{\sqrt{2\pi r}} S_{ij}^\eta(\theta, v). \tag{2.15}$$

Here, η is the crack opening mode - I, II, or III for the in-plane opening, in-plane shearing, and anti-plane shearing mode, respectively; v is the crack speed, and θ the angle from the line drawn from the crack tip in the direction of crack propagation. For crack speeds less than about 40 % of the shear wave speed c_t of the material, the angular variation of stress components is found to differ little from the corresponding equilibrium results. Significant variation appears for higher speeds. In mode I the maximum stress seems to lie in the direction $\theta \approx 100°$ as $v \geq 0.4c_t$ [29]. There is thus some indication of the observed bifurcation of the fast propagating cracks.

The most useful and universal result from the analysis of the problem of non-uniform crack speed is the equation for crack tip motion in mode I,

$$\frac{2E\gamma}{(1-\nu^2)K_I(t,l,0)^2} \approx 1 - \frac{v}{c_R}, \tag{2.16}$$

where l is the crack length, $v = \dot{l}$ the crack speed, and $K_I(t,l,0)$ the stationary ($\dot{l} = 0$) stress intensity factor. Thus, dynamical analysis gives the Rayleigh wave

speed as the maximum speed of crack growth. Also, by drawing an analogy with a mass particle, as the equation of motion is a first order differential equation for a constant crack surface work γ, one can conclude that the crack tip has no effective inertia [29].

In the case of time-independent loading Eq. (2.16) becomes

$$v = c_R(1 - l/l_0), \tag{2.17}$$

where l_0 is a 'constant' depending on fracture energy (and as later experimentally observed, also on crack velocity) [30].

2.2.3 Experimental methods and results

Typically, in an experimental setup for dynamical fracture, stress is applied via externally controlled boundary conditions, and the resulting behaviour of the crack is observed. Some of the quantities measured during crack propagation are the crack's position and velocity, the instantaneous stress field at its tip, and the acoustic emission resulting from its motion. Various optical and photoelastic methods have been developed to measure dynamically the stress intensity factor and energy release rate [33, 34, 35, 36, 37]. Also, the resulting fracture surface can be measured and correlated with any of these dynamical measurements.

The elastic loading of the sample to be fractured can be done statically or dynamically. In static loading either the boundary conditions or applied stress are constant throughout the experiment. In dynamic loading very high loading rates are desirable. A common way to achieve this is by loading a sample which includes a flaw, or a seed for a crack, by collision with a guided projectile. In this way loading rates as high as $\dot{K}_I \sim 10^9 MPa\sqrt{m/s}$ have been achieved [32].

With respect to fragmentation, by far the most relevant experiments on fracture address the velocity and branching of cracks. The most straightforward method for velocity measurement is high-speed photography. To overcome the problem of limited number of frames (~ 30) in high-speed cameras, a method based on using a streak camera was introduced [38]. Variants of resistive methods based on breaking a conductive layer, when a crack is opened, have also been introduced [39, 40, 41, 42].

The linear elastic fracture mechanics has been highly successful in predicting the value of the stress intensity factor at the tip of both stationary and moving cracks, for both static and dynamically applied loads [43]. Likewise, experiments on crack arrest [44] agreed well with the theoretical prediction based on the stress field at a point directly ahead of the crack tip reaching its equilibrium value as soon as the shear (Rayleigh) wavefront has passed [29].

However, the discrepancy between experiments and theory increases with increasing crack velocity for $v > 0.4c_t$. The fundamental problem is that fracture mechanics provides no explanation to the experimentally observed velocity dependence of the fracture energy [38] ($\gamma = \gamma(v)$) in Eq. (2.16)). A rather robust theoretical prediction, when overlooking the divergent behaviour of the left side of Eq. (2.16) as a function of crack velocity v, is that the crack should accelerate and asymptotically approach the Rayleigh wave speed c_R. Experimentally found values for the value at which the crack velocity saturates are, however, far lower than c_R (see Table 2.1 [30]).

Table 2.1: The maximal crack velocities observed in a number of brittle materials [30].

Material	v_{max}/c_R
LiFl	0.63
Rolled tungsten	0.85
Single-crystal tungsten	0.88
MgO	0.88
Weak interface PMMA	0.9
Grooved PMMA	0.8
Glass	0.47-0.66
PMMA	0.58-0.62
Homalite	0.33-0.41

Highest crack velocities have been observed in anisotropic materials. In an experiment performed by Washabaugh and Knauss [45], plates of PMMA were first fractured and then rehealed to form a preferred plane, substantially weaker than the material on its sides. Fracture was performed by impulsively loading the faces of an initial 'seed' crack by means of an electromagnetic loading technique. Velocities of up to $0.9c_R$ were observed. The common feature of crack propagation in anisotropic materials is that microscopic crack branching does not take place [30].

A major effort has been placed on the investigation of the dependence of crack velocity on fracture energy. The continuum theory simply states that energy is supplied by the surrounding continuum to the crack tip - or the very small *process zone* surrounding it - at a rate determined by the speed of elastic waves in the continuum. This statement fails to take into account that the process zone can

actually grow quite large due to microcracking taking place in the vicinity of the crack tip. When the microcracking patterns dominate the crack propagation, the dynamics of the evolution of the process zone can become quite independent of wave propagation in the surrounding elastic body [46]. Microcracking itself is very much dependent on the material, which explains the varying values for v_{max} in Table 2.1. In a nucleation and growth model [47, 48], dynamic crack growth occurs by stress-induced nucleation of micropores or cavities, which then become microcracks and grow and coalesce with each other. It was found that as the stress level increased, more flaws were nucleated farther ahead of the main crack. Growth, interaction, and coalescence of microcracks appears to be the primary mechanism of crack growth in PMMA [46].

When the flow of energy to the crack tip increases sufficiently, the crack is branched into two or more macroscopic cracks. After this bifurcation, single-crack models are, of course, no longer valid. In a series of measurements [41, 42], the velocity of a crack starting at rest was observed to show an initial jump and, after acceleration to a velocity over a certain critical value v_c, oscillations were seen to emerge. The initial jump is understandable as energy flow into and dissipation in the process zone increase abruptly when the crack is nucleated. Velocity can be made to increase gradually by making an initial flaw or small crack from which the the crack starts growing. The value $v_c \approx 0.36 c_R$ was obtained and later found to be independent of sample geometry, sample thickness, applied stress, and the acceleration rate of the crack [30]. Fineberg *et al.* also measured the rms value of the the surface height of fracture surface and found it to be constant for mean velocities $\bar{v} < v_c$, and a monotonically increasing function of $\bar{v}$ for $\bar{v} > v_c$.

An explanation to these instabilities was provided by the experiments by Sharon *et al.* [49]. They observed a sharp transition at $v = v_c$ from a state having no branches to a state where both a main crack and daughter cracks are observed. Microbranching was found to be responsible for both the structure of the fracture surface and the fluctuations in the crack velocity.

As a crack accelerates, the energy released from the elastic energy stored in the surrounding material is used for the creation of new fracture surface. When the velocity of the crack reaches v_c, the energy flowing into the crack tip is divided between the main crack and its daughter cracks formed by branching. Thus, there is less energy available for each crack and the velocities of the cracks diminish. Apparently the main crack screens its daughter cracks, which thus have a finite lifetime. The main crack can 'outrun' the daughter cracks as it has the geometrical advantage of straight-line propagation. As the daughter cracks die, there is more energy available for the main crack and it begins to accelerate again, until the scenario described above repeats itself [30].

Sharon *et al.* have shown that, at a given mean velocity in PMMA, the lengths of and distances between consecutive daughter branches are characterised by log-normal distributions, whose mean and standard deviations are linearly increasing functions of the mean crack velocity [50]. Although individual branch lengths seem to vary randomly, the average branch profile can be very accurately described in both PMMA and glass by a power-law form [50, 51],

$$y = 0.2x^{0.7}, \tag{2.18}$$

where x and y are the directions parallel and perpendicular to the direction of the main crack propagation, respectively. The origin is taken to be the point at which a daughter branch begins. As this expression is identical for two such highly different materials, one might conjecture that it is universal. The assumption is further supported by observations of branch profiles in polystyrene [52].

Comparing the form Eq. (2.18) with the experimental data for branching angles, and taking into account the distance at which this angle was measured, Fineberg and Marder [30] found excellent agreement. They suggested that there is a smooth transition between microscopic and macroscopic crack branch profiles in brittle materials and that the branches at length scales < 1000 μm exhibit a high degree of universality. Thus, presumably, the criterion for the formation of macroscopic crack branches coincides with the onset of the microbranching instability [30]. The onset of macroscopic branching was indirectly inferred from experiments to occur at $v \approx 1.7v_c$ [50].

2.3   Conceptual models for fragmentation

Even before Kolmogorov's argument for log-normal fragment-size distribution (FSD) [21], several attempts in the realm of statistical fragmentation had been taken. One of the earliest of the kind is the one by Lienau [53]; even he refers to some similar earlier studies in Japan [54] and to literature in mineral dressing. Lienau discussed the geometric statistical problem of randomly distributed points on a line and the distribution of fragment lengths created by this random partitioning. The relevance of Poisson distribution in describing these random points was brought up by him.

There is general agreement over how geometric statistical fragmentation is applied in one dimension, and we outline the main points here. By starting from an initial Poisson distribution of points on an infinite line, *i.e.* probability of finding n points in a length l is $P(n|l) = (N_0 l)^n e^{-N_0 l}/n!$, where N_0 is the average number of points per unit length, Lienau arrived at an exponential cumulative fragment number per unit length [55]

$$N(l) = N_0 e^{-N_0 l}. \tag{2.19}$$

One can show quite easily that for a line of finite length l_0 the corresponding equation reads

$$N(l) = N_0 \left(1 - \frac{l}{l_0}\right)^{N_0 l_0 + 1}. \tag{2.20}$$

The two cumulative fragment numbers per unit length can also easily be shown to be equivalent when $l \ll l_0$.

After Lienau, Mott extended the geometric concept of random points on a line to random fragmentation of a two-dimensional region, and suggested a distribution (which fitted the data he had access to) of the cumulative number of fragments in the form [56]

$$N(s) = N_0 e^{-\sqrt{2N_0 s}}, \tag{2.21}$$

where N_0 is the average number per unit area and s is the fragment area. Mott and Linfoot tried then to justify this form by giving an analytic solution for the distribution of fragment areas formed by the random arrays of horizontal and vertical lines of equal density in an infinite area [56]:

$$N(s) = 2N_0 \sqrt{N_0 s} \; K_1(2\sqrt{N_0 s}). \tag{2.22}$$

Here, K_1 is a modified Bessel function. The analytical solution and the Mott distribution agree reasonably well, except for small s, as verified in [55]. Mott and Linfoot argued that the Mott distribution is probably better than the solution for the problem where lines are drawn only from two sets of parallel lines. For fragments of equivalent shape but of random size, the Mott distribution is exact [55].

Based on a large set of experimental data and on their numerical investigation of geometric fragmentation problems, Grady and Kipp suggested that, in complete analogy to the 1D case, Eq. (2.19), fragment sizes in 2D fragmentation are determined by breaks distributed randomly on scalar measure s of area. These 'points' then define a Poisson variable, and the cumulative fragment number distribution is given by

$$N(s) = N_0 e^{-N_0 s}. \tag{2.23}$$

This expression is called a linear exponential distribution [55].

The work referenced above considered fragmentation as a geometric statistical process. Common to all of them, fragment size distribution (FSD) was of some kind of exponential form. There was however a derivation within geometric statistics, which included some physical assumptions, that gave a power-law form for FSD, *i.e.* the one due to Gilvarry [14]. He introduced it to explain the experimental results by himself and Bergstrom [8]. As this result is closely connected to the results presented in this work, we will briefly outline its derivation here and make reference to the related work by Grady and Kipp [55].

Gilvarry assumes that cracks start either from newly nucleated flaws or from some of the initial flaws (hence called *activated*) and propagate in the material without branching until stopped by the boundary of the specimen or by an existing crack in its path. The original specimen is considered infinitely large, so that there are no surface flaws.

The internal flaws are assumed to be randomly distributed in the specimen with a low enough concentration to conform with a Poisson distribution. That is to say, a set of M points is randomly distributed over a domain of extent T such that

$$\lim_{M,T\to\infty} \frac{M}{T} \to \gamma, \tag{2.24}$$

where γ is a finite constant. Under this condition, the probability $P(n|t)$ of points falling in a subdomain of extent t is given by the Poisson distribution

$$P(n|t) = \frac{e^{-\gamma t}(\gamma t)^n}{n!}. \tag{2.25}$$

When an initial flaw is activated, two contiguous surfaces result from crack propagation, each of which contains flaws arising from intersection of these surfaces with other initial flaws. A new fracture surface can arise by activation of such a flaw on a surface. Similarly, an edge formed by intersection of two fracture surfaces may contain flaws distributed along a line, activation of which can yield new fractures. Gilvarry refers to the three types of flaws as volume, facial, and edge flaws, respectively. Fragmentation is then assumed to proceed by activation of a set of all three types of flaws.

Poisson distribution is assumed to hold for *activated* flaws as well as the rest of the initial flaws. The first flaws are assumed to be activated by an externally applied stress, which is instantly and permanently removed when the first cracks begin to propagate. Subsequent flaws are then activated by stress waves produced by propagation of the prior ones. Gilvarry states that the removal of the external stress permits fragmentation to be controlled entirely by the postulated random distributions of activated flaws in the original specimen. We comment on this point later in Chapter 4. Gilvarry defines constants γ_v, γ_s, and γ_l as the mean volume, areal, and linear densities of activated flaws of volume, facial, and edge type, respectively.

In defining a differential element the total edge length, face area, and volume of the fragment are increased from l to $l+dl$, from s to $s+ds$, and from v to $v+dv$, respectively. The probability of having at least one activated flaw of one of the three types in this element is

$$P(1|dl, ds, dv) = P(1|dl) + P(1|ds) + P(1|dv), \tag{2.26}$$

since the activation of the different types of flaws are mutually exclusive. The probability that no activated flaw is contained in the fragment, is given by

$$P(0|l, s, v) = P(0|l)P(0|s)P(0|v). \tag{2.27}$$

Thus, the probability $dp(l, s, v)$ of formation of a fragment with total edge length, total face area, and total volume in the ranges $[l, l + dl]$, $[s, s + ds]$, and $[v, v + dv]$, respectively, is given by

$$dp(l, s, v) = P(0|l, s, v)P(1|dl, ds, dv) = e^{-Q}dQ, \tag{2.28}$$

where $Q = \gamma_l l + \gamma_s s + \gamma_v v$.

The number $dn(l, s, v)$ of fragments with total edge length, total face area, and total volume in the fore mentioned ranges can now be expressed in the form

$$dn(l, s, v) = q(l, s, v)dp(l, s, v), \tag{2.29}$$

where $q(l, s, v)$ is the *a priori* number of fragments with the values l, s, and v.

Gilvarry then proceeds to claim that, given the volume V_0 of the initial specimen, q is fixed by

$$q = V_0/v, \tag{2.30}$$

and is independent of l and s. Accordingly, he then finds that

$$dn(l, s, v) = V_0 v^{-1} e^{-Q} dQ. \tag{2.31}$$

This expression should thus be the general form for the distribution function of fragment sizes in a fracture in which the distributions of edge, facial, and volume flaws are independent Poisson distributions. Gilvarry finds that for the scenario described above the edge flaw contribution dominates, so that $Q \approx \gamma_l l$ [14].

The numerical work done by Grady and Kipp [55] addressed many of the suggested analytical models for FSD's, including that of Gilvarry's. For all cumulative FSD's obtained from the numerically implemented models, they found close agreement with the linear exponential distribution, Eq. (2.23). Thus, there was apparently no trace in FSD of power-law form.

Let us analyse a bit more closely Gilvarry's derivation. We can find no justification for the assumption made in Eq. (2.30) for the form of the *a priori* number of particles q. The term v^{-1} is thus effectively put in by hand and, as a result of this, Eq. (2.31) is found for the distribution of fragment sizes. Without this assumption Gilvarry would have obtained a purely exponential form for FSD, in agreement with the results in [55].

Unlike for statistical fragmentation in 1D, there seem to be different views in dimensions greater than one. Typically, models of fragmentation are in general hierarchical ones, which means that a large piece first breaks into smaller ones, that may then break further. The reason is obvious: hierarchical process is conceptually easy allowing one to write down formal equations for the development of fragment sizes. Also, nothing prevents one from making such an assumption as there seems to be no data, experimental or numerical, on the time evolution of fragmentation.

Marsili and Zhang [15] introduced a hierarchical analytical model without using a specific breaking mechanism. For simplicity, the assumption of fragments breaking into two smaller fragments at each level was made. In the model, breaking of an object is determined by its energy density E/V: If $E/V > 1$, the object breaks into two pieces of energy ϵ and $E - \epsilon$, and volume v and $V - v$, respectively. These are again subject to the energy density criterion for breaking further into two. The process is repeated for an arbitrary number k of levels.

These authors assume a uniform distribution in energy and set $q(\epsilon, v|E) = E^{-1}\phi(v)$, where $q(\epsilon, v|E)$ is the probability that the energy and volume of an element are in the ranges $[\epsilon, \epsilon + d\epsilon]$ and $[v, v + dv]$, respectively, and $\phi(v)$ is the volume distribution with an additional symmetry requirement $\phi(v) = \phi(1 - v)$, obviously for analytical reasons. An iteration relation for the distribution p of the energy density x is constructed,

$$p_{k+1}(x) = \int_1^\infty p(x|E)p_k(E)dE, \qquad (2.32)$$

where $p_k(E)$ is the energy distribution at level k with the total energy E, and $p(x|E)$ is the energy density distribution of the object unstable against fragmentation. By writing the asymptotic limit in the form

$$p_\infty(x) \sim Ax^{-\gamma}, \qquad (2.33)$$

the exponent can be solved from

$$\gamma = \int_0^1 v^{1-\gamma}\phi(v)dv. \qquad (2.34)$$

The physical solution for any ϕ is then obtained for $\gamma = 1$. After some additional approximations a power-law form for volume (mass) distribution of stable fragments is obtained,

$$W(V) \sim V^{-\alpha-1}, \qquad (2.35)$$

where $\alpha = 1$ in the limit of infinite range for volumes. In this model α also depends on the initial energy E_0. As E_0 increases α increases until it reaches the universal value 1. Because $V = r^D$ and $N(r) = \int_V^\infty W(V')dV' \sim r^{-d}$, where D is spatial

dimension and d the power-law exponent, the relation $d = D\alpha$ can be written. Thus an upper limit D for d is obtained in accord with all the data referenced in [18].

The value of the model presented above lies again in the conceptual developments made. However, despite that the authors set as their goal to formulate a scheme which produces a power-law FSD without referring to any specific fracture mechanism, the exponent α is rendered dependent upon these mechanisms (like the number of resulting fragments at each level) and initial conditions (E_0, V_0). The dependence of α on E_0 is however questionable: In real fragmentation processes the power-law exponent does not simply saturate to universal value as the input energy is increased. On the contrary, the power-law form disappears at values high enough for E_0, so that the mass range in which the scale-invariant form appears is reduced at large masses. The difficulty with this kind of modelling is related to the lack of knowledge of the actual fragmentation process.

The conceptual model introduced by Kadono and Arakawa [12] serves as an example of a mere probabilistic hierarchical scheme without any reference to physical parameters, such as energy. It will also play a role in the analysis below of the results obtained from our simulations. This model was introduced to explain results obtained from an experiment, where crack propagation within thin glass plates under high shock loading induced by a projectile was observed using a high speed camera.

The process was proposed for 2D but it can easily be adopted in 3D as well. First, a square with unit area is divided into b^2 subsquares of side $1/b$. At the second step b^2p subsquares, where p is the fraction of the subsquares which will be further fragmented, will each be divided into b^2 equal subsquares of side $(1/b)^2$. By repeating the procedure, a collection of an infinite number of fragments of various sizes is obtained. The number of fragments with length $r_n = (1/b)^n$ is $(pb^2)^{n-1}(1-p)b^2$. The cumulative number of fragments larger than r_n can now be written as

$$\begin{aligned} N(> r_n) &= (1-p)b^2 + pb^2(1-p)b^2 + \ldots + (pb^2)^{n-1}(1-p)b^2 \\ &\sim (pb^2)^n = r_n^{-\gamma}, \end{aligned} \tag{2.36}$$

where $\gamma = \ln(b^2p)/\ln b$. This simple model will be used later in Chapter 4 in more detail.

In the models outlined above the emphasis is on the statistical aspects of fragmentation. Physical parameters were scarcely considered. The implicit assumption was that fragmentation takes place in a fashion by which the whole specimen is fragmented but shattering does not occur. A characterisation of fragmentation as a function of impact energy was done by Kun and Herrmann [7]. With a 2D dynamical model of deformable, breakable, granular solids they were able to show that there is a sharp transition as a function of impact energy between two final states, a *damaged* and a *fragmented* state, as defined in Chapter 1. They chose the di-

mensionless ratio of the energy impact and the binding energy of the sample as the control parameter, and the mass of the largest fragment divided by the total mass as the order parameter. By studying the behaviour of the fragment mass distribution in the vicinity of the transition point, and its dependence on the finite particle size, they gave numerical evidence that the transition point behaves as a critical point and is analogous to a continuous phase transition. In all subsequent simulations and analysis presented in this work fracture occurs close to this transition point.

2.4   Some relevant experimental results

There is a vast amount of experimental data on fragmentation. A review of the results up to 1986 can be found in [18]. Of the later experiments we make explicit reference to only three that have high relevance to the present study.

Oddershede *et al.* performed a series of experiments on objects of different shapes [9]. The objects were cast of gypsum by pouring liquid gypsum into an open mould of desired shape, thereby minimising stresses and strains in the objects. The dried objects were then fragmented by throwing them onto a hard floor. The mass of each fragment was then measured, those larger than 10^{-2} g by an electronic scale and those in the range $[10^{-3}, 10^{-2}]$ by an analytical balance. To check possible dependence of the way the impact was given, identical objects were struck in different ways, but no difference in the resulting distributions was seen. Also, experiments were performed with objects of different materials (frozen steric paraffin, soap and peeled potato), but no dependence on material was observed.

As measurements yield single events, the total number of fragments with masses larger than or equal to s, $N(s)$ rather than the continuous probability $n(s)$ was measured,

$$N(s) = \frac{1}{s} \int_s^\infty n(s')ds'. \qquad (2.37)$$

Measured distributions were found to be of the form

$$N(s) \sim s^{-\beta} \exp(-s/s_0), \qquad (2.38)$$

where s_0 was interpreted as a characteristic finite-size cutoff mass. The exponent β was found to depend on the effective dimension of the object defined by the authors such that

$$d_m = 1 + 2(ab + ac + bc)/(a^2 + b^2 + c^2), \qquad (2.39)$$

where a, b, and c are the lengths of the three sides of the object.

The dependence of exponent β on this dimension, as found in Ref [9], is shown in Table 2.2.

Table 2.2: Experimental values for β [9].

d_m	1	2	3
β	1.0 ± 0.1	1.2 ± 0.1	1.55 ± 0.1

Meibom and Balslev performed further experiments of similar kind and, besides confirming the observations made by Oddershede *et al.* [9], concluded that exponent β depends on the dimension of the original object *on the length scale of the fragment considered* [10]. To this date, however, no explicit argument exists for the observed dimensional dependence of β.

Katsuragi *et al.* [57] performed experiments in some sense complementary to those outlined above. A glass tube was placed between a hard stage and a plate, both of stainless steel. The stage was fixed by placing heavy weights on it. A cylindrical brass weight with a flat and even bottom surface was dropped on the stainless steel plate vertically. A planar failure wave thus propagated to the glass tube from the cross section of the tube. Consequently, the glass tube was cleaved by the impact. Unlike in the experiments referenced above, the whole fragmentation process is thus ensured to take place as cleavage in 2D. The power-law form $N(s) \sim s^{-0.5}$ was obtained over two orders of magnitude in fragment size.

Chapter 3

Method and Numerical Models

3.1 Lattice model and dynamics

Fragmentation of a brittle material was modelled using a lattice of mass sites at discrete positions. Masses formed a square lattice and were each connected to their nearest neighbours by massless, elastic beams of square cross section w^2, length l, and Young's modulus E. Beams deform elastically according to the matrix equation

$$\vec{F} = \mathbf{T}^T \mathbf{K} \mathbf{T} \vec{U}, \tag{3.1}$$

where vector $\vec{F} = F(f_x^1, f_y^1, f_x^2, f_y^2, l_x^1, l_y^1, l_x^2, l_y^2)$ contains the forces $\vec{f^i}$ and angular momenta $\vec{l^i}$ acting on the two ends ($i = 1, 2$) of the beam, $\mathbf{T}$ is the rotation matrix transforming the beam's local coordinate system, whose x-axis is chosen to be the beam axis, into the global coordinate system of the lattice, and $\vec{U}$ is the displacement vector of a lattice site. $\mathbf{K}_l$ is the stiffness matrix in the local coordinate system given by

$$\mathbf{K}_l = \begin{pmatrix} \frac{EA}{l} & 0 & 0 & \frac{-EA}{l} & 0 & 0 \\ 0 & \frac{12EI}{l^3} & \frac{6EI}{l^2} & 0 & \frac{-12EI}{l^3} & \frac{6EI}{l^2} \\ 0 & \frac{6EI}{l^2} & \frac{4EI}{l} & 0 & \frac{-6EI}{l^2} & \frac{2EI}{l} \\ \frac{-EA}{l} & 0 & 0 & \frac{EA}{l} & 0 & 0 \\ 0 & \frac{-12EI}{l^3} & \frac{-6EI}{l^2} & 0 & \frac{12EI}{l^3} & \frac{-6EI}{l^2} \\ 0 & \frac{6EI}{l^2} & \frac{2EI}{l} & 0 & \frac{-6EI}{l^2} & \frac{4EI}{l} \end{pmatrix},$$

in which $A = w^2$ and $I = \frac{w^4}{12}$ is the moment of inertia introduced by the masses at the lattice sites. Columns 1 and 4 in $\mathbf{K}_l$ give the linear force elements exerted on the two ends of the beam along its axis, and columns 2 and 5 give the corresponding force elements in the y direction. Columns 3 and 6 give the elements of angular momenta exerted on the two ends. The forms of the elements can be calculated starting from the equilibrium equations for the beam.

The lattice dynamics are governed by discretised Newton's equations of motion, which, starting from the continuum equations $\mathbf{M}\ddot{\vec{U}} + \mathbf{C}\dot{\vec{U}} + \mathbf{K}\vec{U} = \vec{F}$ and definitions $\dot{\vec{U}} = [\vec{U}(t+\Delta t) - \vec{U}(t-\Delta t)]/(2\Delta t)$ and $\ddot{\vec{U}} = [\dot{\vec{U}}(t+\Delta t) - \dot{\vec{U}}(t)]/(\Delta t)$, can be written as

$$
\left[\frac{\mathbf{M}}{\Delta t^2} + \frac{\mathbf{C}}{2\Delta t}\right]\vec{U}(t+\Delta t) = \left[\frac{2\mathbf{M}}{\Delta t^2} - \mathbf{K}\right]\vec{U}(t) \tag{3.2}
$$
$$
- \left[\frac{\mathbf{M}}{\Delta t^2} - \frac{\mathbf{C}}{2\Delta t}\right]\vec{U}(t-\Delta t) + \vec{F}(t).
$$

Here $\mathbf{M}$ is the mass matrix, $\mathbf{C}$ is the damping matrix, both of which are diagonal, $\mathbf{K}$ is the global stiffness matrix, and $\vec{F}$ contains the external forces exerted on the lattice sites.

The disorder is introduced into the system by either distorting the lattice by a controllable amount or by defining Young's moduli whose magnitudes randomly vary from beam to beam. The fluctuation of the moduli around a nominal value can again be controlled. The beams break instantaneously and irreversibly thus rendering the stiffness constants independent of strain or strain-rate.

The lattice model is thus completely generic and unrelated to any specific material. This is justified by the observed universal behaviour of brittle fragmentation, regardless of material differences [9]. The square lattice obviously suffers from anisotropy, unlike *e.g.* the Voronoi lattice. However, in contrast with Voronoi lattice, its advantage is the easiness with which disorder can be controlled.

3.2 Imposing periodic boundary conditions

In order to eliminate the boundary effects arising from an elastic loading of the inevitably finite lattice, we implemented periodic boundary conditions in the algorithm. To accomplish this so that any constraint imposed on the lattice via elastic loading be eliminated, it is necessary to introduce extra degrees of freedom, through which the loading can be performed. As will be seen, this is not trivial. On the other hand, all the systems on which fracture experiments are performed are certainly constrained by the loading. Thus, although desirable to get rid of these loading constraints in order to observe only the features inherent to fragmentation, it is also of interest merely to eliminate the boundary effects due to non-periodic boundary conditions. This way the characteristics arising from the constrained strain can be identified. To this end, we implemented periodic boundary conditions in two ways, one that preserved loading constraints and another that eliminated them. The introduction of extra degrees of freedom in the second case enabled us to simulate two-dimensional systems in three-dimensional space.

3.2.1   Minimal model

In the first method, coined the *minimal model*, loading is performed by expanding the periodic box up to a maximum strain ϵ_m ($\epsilon(t) = \epsilon_m \sin^2(\omega t)$, for $t \le \pi/(2\omega)$, $\epsilon(t) = \epsilon_m$, otherwise). In the discrete Newton's equations of motion the inertial effects related to the expansion of the periodic box are easily removable. The inertia created in the elastic relaxation of the system is damped by a 'viscous' damping term in the equations of motion. Fragmentation is allowed only after the maximum strain is reached. A 2D version of this model was used in the simulations made for Publications II and III.

3.2.2   Scaling dynamics

The method which is free from any extra constraints imposed via elastic loading requires slightly more elaboration. To expand the surface without adding kinetic energy in the direction of the lattice surface, additional degrees of freedom need to be brought into the system. For each lattice site i an extra parameter, $SC_i(t)$, depicting the local magnitude of expansion or contraction of the lattice is introduced. The introduction of expansion variables independent of the dynamical variables associated with the dynamics of the surface on which periodic boundary conditions are imposed, implies a close analogy with a curved two-dimensional surface expanding in 3D space. Thus the expansion, or scaling, of the surface can be visualised as an increase in the surface radius of curvature, $R_i(t)$, determined locally at each site. The scaling factors of the displacements in Eq. (3.3) can thus be defined as

$$SC_i(t) = \frac{R_i(t)}{R_i(0)} = \frac{R_i(0) + \delta R_i(t)}{R_i(0)}, \tag{3.3}$$

where $R_i(0)$ is the initial radius of curvature and $\delta R_i(t)$ is the accumulated change (sum of changes at previous time steps) of the radius at time t.

As imposing constraints is to be avoided, we let the radius parameter perform Newtonian dynamics. Arbitrary masses can be associated with the radius parameters at different lattice sites, but sticking to the analogy with the curved expanding surface it is natural to define it equal to the lattice site mass m. As this radius is orthogonal to the lattice surface at each lattice site and obeys Newtonian dynamics, we have effectively extended the system by two extra degrees of freedom per lattice site - namely position and velocity in the direction of the outer normal of the surface of the 'torus' thus formed. The radius parameter obeys Newtonian dynamics according to Eq. (3.3) with the forces determined by projecting the elastic forces on the curved surface of the torus into the direction perpendicular to the surface. The magnitude of this projected force at each time step can be calculated from the torus

geometry (Eq. (3.9) below). This force then directly affects the position of the mass site in the radial z direction and, in a manner explained below, the position in the surface directions x and y as well,

As the scaling of a site is an extra parameter, its relation to the site's displacement, and velocity, and to forces in the surface directions, have to be explicitly defined in the dynamics. In all computations that contribute to the forces exerted on the mass sites, the displacements need to be given at correct scaling levels. In other words, at each step in the algorithm, the displacements of the neighbouring sites need to be transformed to values corresponding to a judiciously determined scaling level. Of the scaling levels of two neighbouring sites, the one closer to some predetermined level is chosen as the reference scaling $SC_{\langle i,j\rangle}^{ref}(t)$ based on which the calculation is done. The mentioned predetermined level can be chosen to be the scaling level averaged over all sites, as in Publication I, or it can be defined as a local average around the interacting sites. The latter was used in Publication IV. The displacement of the site that is farther from this level, say i, is transformed so that its displacement along the surface corresponds to scaling of the site closer to the predetermined level, say j. The latter was thus chosen as $SC_{\langle i,j\rangle}^{ref}(t)$. The transformed displacement for site i can thus be written as

$$\vec{U}_i^{tr}(t) = [SC_{\langle i,j\rangle}^{ref}(t) - 1]\vec{XY}_i + \frac{SC_{\langle i,j\rangle}^{ref}(t)}{SC_i(t)}[\vec{U}_i(t) - \vec{U}_i^0(t)]. \tag{3.4}$$

Here $\vec{XY}_i$ denotes the initial, unscaled position of the ith lattice site, $\vec{U}_i(t)$ the displacement of the ith site at its present scaling level $SC_i(t)$, and $\vec{U}_i^0(t)$ the displacement of this site due only to the scaling of the lattice, *i.e.*, with the part that results when the surface dynamics is excluded,

$$\vec{U^0}_i(t) = [SC_i(t) - 1]\vec{XY}_i. \tag{3.5}$$

Obviously Eq. (3.4) could also be written more compactly. The given form proved to be numerically the most stable.

The transformation to the displacements according to Eq. (3.4) is depicted in Fig. 3.1. The relative displacements of the sites i and j in the direction normal to the surface are calculated using the radius of curvature and the difference in the scaling factors $SC_i(t)$ and $SC_j(t)$ (see the last term in Eq. (3.9)).

After having transformed the displacements to the same scaling by Eq. (3.4), the periodicity of the scaled lattice needs to be taken into account. For all the sites whose connecting beams cross a periodic boundary, the above transformed displacement needs to be further transformed such that

$$\begin{aligned}\vec{U}_i^{tr'}(t) &= \vec{U}_i^{tr}(t) - [SC_{\langle i,j\rangle}^{ref}(t) - 1]\vec{XY}_i + \\ &\quad + \{\vec{XY}_{i',D=0} - \Delta\vec{XY}_{D=0} + \vec{XY}_i - \vec{XY}_{i,D=0}\}[SC_{\langle i,j\rangle}^{ref}(t) - 1]. \tag{3.6}\end{aligned}$$
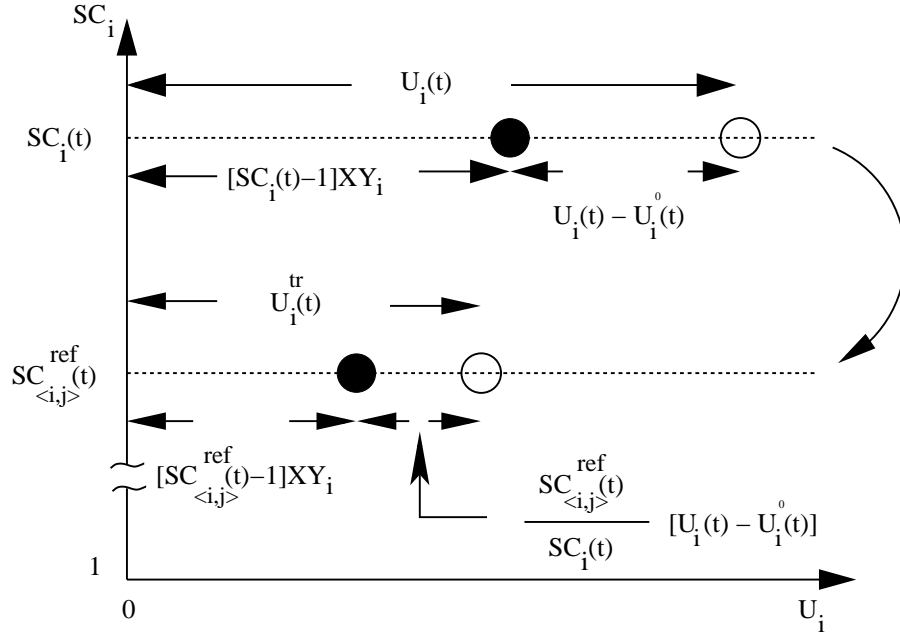
Figure 3.1: Schematic diagram depicting the transformation of displacements to another scaling level. The vertical axis depicts the scaling value SC_i and the horizontal axis the displacement relative to the initial position XY_i with $SC_i(t=0) = 1$. It is assumed here that $SC_i > SC_j$ and that, of the neighbouring sites i and j, the scaling factor of the latter is closer to the scaling averaged over the whole lattice. Thus, the force computation is to be performed at the scaling level $SC_{\langle i,j \rangle}^{ref}(t) = SC_j(t)$, and the displacement $\vec{U}_i(t)$ is transformed to the value $\vec{U}_i^{tr}(t)$ corresponding to this scaling. It is now evident how the mere scaled initial coordinates $\vec{U^0}_i(t) = [SC_i(t) - 1]\vec{XY}_i$ and the displacements caused by the dynamics $\vec{U}_i(t) - \vec{U}_i^0(t)$ are rescaled separately. The vector notation is omitted in the figure as it depicts displacements in one dimension.

Through this equation the displacement of lattice site i is transformed to correspond to the displacement it would have, were it located in the neighbouring periodic cell so that it would lie next to its neighbouring site i' on the opposite boundary in the present (or actual) cell. By $D \in [0,1]$ we denote the effective strength of disorder. $\vec{XY}_{i,D=0}$ denotes the initial unscaled position of the lattice site i with the quenched disorder part excluded ($D = 0$), and $\Delta \vec{XY}_{D=0}$ is the distance between neighbouring lattice sites at their initial positions with no disorder. The first two terms give the properly scaled displacement from the initial position. The remaining part then adds to this the new position calculated from the initial position in the adjacent periodic cell with proper scaling. Again, the transformation could be written more compactly, but the form given above proved to be the numerically most stable one. The transformation of displacements from one periodic cell to another proved to be the operation most prone to numerical instability, so using the best possible form is important.

To determine whether a beam after the last time step should break or not, its length $L_{\langle i,j \rangle}(t)$ has to be computed including the radial component and taking into account the periodicity of the lattice,

$$
\begin{aligned}
L_{\langle i,j \rangle}(t) &= |\vec{XY}_i - \vec{XY}_j - PRX_{\langle i,j \rangle}L_x - PRY_{\langle i,j \rangle}L_y + \\
&+ \vec{U}_i^{tr'}(t) - \vec{U}_j^{tr'}(t) + [SC_j(t) - SC_i(t)]\vec{R}_i(0)|.
\end{aligned}
\tag{3.7}
$$

$PRX_{\langle i,j \rangle}$ is a factor whose value is zero if the beam does not cross a periodic boundary, and one otherwise. L_x and L_y are the lengths of the unscaled lattice in the x and y directions, respectively.

The load, proportional to the relative strain of the beam, is then calculated as

$$
Load_{\langle i,j \rangle}(t) = \frac{L_{\langle i,j \rangle}(t) - L_{\langle i,j \rangle}(0)}{L_{\langle i,j \rangle}(0)},
\tag{3.8}
$$

and is compared with a preset threshold for irreversible breaking of the beam.

As mentioned, the force exerted on lattice site i, projected in the direction perpendicular to the surface, is determined based on the geometry of the curved surface,

$$
\begin{aligned}
F_i^p(t) &= Ew^2 \left| \frac{L_{\langle i,j \rangle}(t) - L_{\langle i,j \rangle}(0)}{L_{\langle i,j \rangle}^0} \right| \{ sgn(SC_{\langle i,j \rangle}^{ref}(t) - 1.0) \frac{L_{\langle i,j \rangle}(t)}{2SC_{\langle i,j \rangle}^{ref}(t)R_i(0)} + \\
&+ [SC_i(t) - SC_j(t)] \frac{R_i(0)}{L_{\langle i,j \rangle}(t)} \}.
\end{aligned}
\tag{3.9}
$$

The first term on the right side of the equation gives the force due to the curvature and the remaining part gives the contribution due to the difference in the scaling
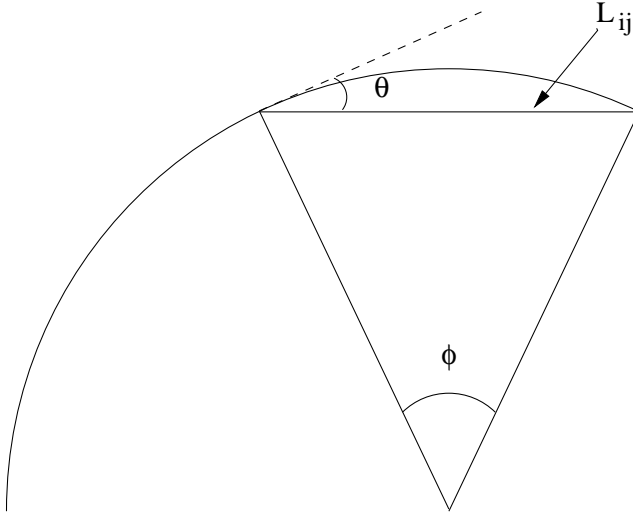
Figure 3.2: Schematic picture of a beam L_{ij} on the curved surface. The length of the beam with respect to the radius of curvature is exaggerated in order to make angles visible.

parameters (*i.e.* the distance in the direction perpendicular to the curved surface) of neighbouring lattice sites i and j. $sgn(SC^{ref}_{\langle i,j \rangle}(t) - 1.0)$ gives the direction of the force due to the curvature.

A schematic picture of a (scaled) beam L_{ij} is given in Fig. 3.2. From the geometry the force induced by surface curvature can be calculated as follows: The initial beam length can be written as $L_{0ij} = \sqrt{(x_{0i} - x_{0j})^2 + (y_{0i} - y_{0j})^2 + (z_{0i} - z_{0j})^2}$. The force exerted on mass i, say, is $\vec{F} = k\Delta\vec{U}$, where k can be taken as constant due to the small relative strains before the beam breaks: $k = (Ew^2)/L_{ij} \approx (Ew^2)/L_{0ij}$, and $\Delta U = \sqrt{(x_{0i} - x_{0j})^2 + (y_{0i} - y_{0j})^2 + (z_{0i} - z_{0j})} - L_{0ij}$. Now $\theta = \phi/2$ and the force components parallel and perpendicular to the curved surface are $F^{par} = F\cos\theta$ and $F^{orth} = F\sin\theta$, respectively. Now $L_{ij}/2 = R\sin(\phi/2) = \sin\theta$, so that $\theta = \arcsin(L_{ij}/(2R))$, where R is the radius of curvature. Hence, $F^{orth} = FL_{ij}/(2R)$. This form, given for the curvature induced part in Eq. (3.9), was used in order to follow the curved surface analogy. In principle any form for the orthogonal force could be used, as long as it keeps the dynamics of the expanding/contracting surface stable.

The radius parameter at time step $t + \Delta t$ can now be determined from the one

at t using a discretised Newton's equation for the radius parameter,

$$[\frac{m_i}{\Delta t^2} + \frac{C_i}{2\Delta t}]R_i(t + \Delta t) =$$
$$[\frac{2m_i}{\Delta t^2} - \mathbf{K}]R_i(t) - [\frac{m_i}{\Delta t^2} - \frac{C_i}{2\Delta t}]R_i(t - \Delta t) + F_i^p(t) + F_i^e(t), \qquad (3.10)$$

where $F_i^e(t)$ is the external force applied on lattice site i.

Unlike in the case of constrained dynamics, loading of the system described above can be realised by having $F_i^e(t) \neq 0$, which induces more instability to crack dynamics (see discussion after Eq. (2.2)). In the simulations made for Publication IV, $F_i^e(t)$ was set to zero and an initial impulse for expanding the system was given by setting $R_i(-\Delta) = -A \cdot \Delta t$, with A a constant, and letting the system go. The curved elastic beam lattice then performed unconstrained dynamics.

The force calculations in connection with the transformations of displacements to different scaling levels are based on linear approximations, so the model is valid only for brittle materials not exhibiting plasticity.

Chapter 4

Results

4.1 Lattice elastodynamics

Differences in the static properties of the discretised lattice model and the continuum system were shown to be negligible by checking energy conservation in a loaded system, and by comparing the static stress field obtained for a 2D plate with a hole in the middle with the corresponding analytical solution. Wave dynamics as given by the discrete model was also seen to conform with excellent accuracy with the continuum dynamics by comparing the transverse and longitudinal wave speeds in the beam directions (see Publication I).

The effect of discretisation and anisotropy of the lattice, however, showed in crack propagation. The measured speed of crack propagation, v, slightly exceeded the theoretical upper limit, the Rayleigh wave speed v_R, in the absence of micro-branching. In Publication I v_R was given based on a 3D consideration. As pointed out, the parameter ξ in Eq. (2.14) has however a slightly higher value in 2D. This would take v a bit farther away from v_R. On the other hand, v was measured in a soft direction of the anisotropic lattice, which partly explains its apparently somewhat too large a value as stress enhancement is expected in soft directions. In principle, in a discrete ordered lattice infinite crack velocity can be attained as adjacent beams may break during a single time step.

Crack velocities for two strain-rate values are shown in Fig. 4.1. The instability due to the discreteness of the lattice increases with increasing strain rate. It appears as larger oscillations in the crack velocity for larger strain rates. Thus, at larger strain rates the first beams break at lower strain values so that crack propagation is strain controlled, which explains the lower value for v in Fig. 4.1A than in Fig. 4.1B. At sufficiently small strain rates the crack starts propagating at a fairly small strain,
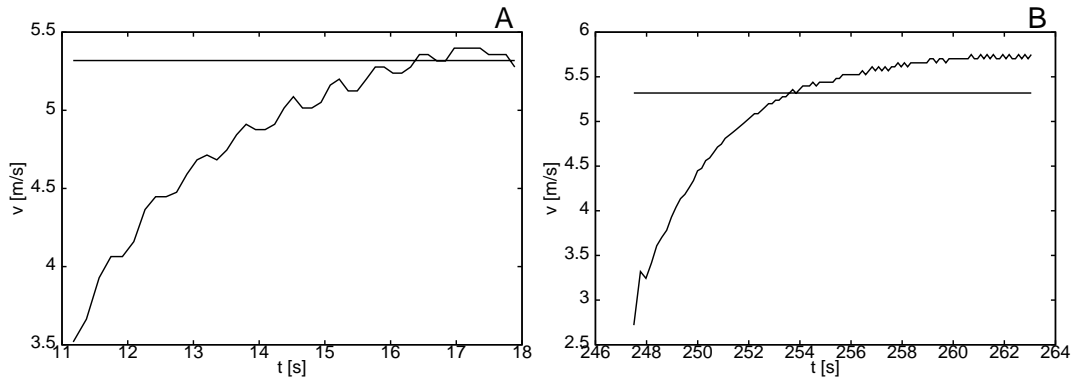
Figure 4.1: Crack velocity as a function of time for $W = 1$ and $L = 1/\sqrt{2}$. The straight lines show the velocity of the transverse wave c_T. In A the strain rate is $1.06 \cdot 10^{-3} m/s$, and in B it is $7.07 \cdot 10^{-5} m/s$.

which increases while crack accelerates to its maximum attainable velocity. Then crack propagation is no longer controlled by the strain rate.

Although the mechanism behind the observed velocity oscillation in a discrete lattice is different from the one causing the experimentally observed velocity oscillations, namely microbranching [49] (see Section 2.2.3), their similar appearance is understandable. In the case of microbranching, the crack can be thought to be accelerated in those intervals when no microbranching occurs. Elastic energy is expended locally at the crack tip when a microbranch is generated. When the microbranch finally stops, the strain rate has increased, and the velocity of the crack increases until another microbranch is generated. In our discrete lattice elastic energy is expended in breaking beams. After a beam or beams are broken, elastic energy is stored a while in the vicinity of the crack tip until several beams may break at the same or consequent time steps, thus producing an increased velocity.

When multiple cracks were present, velocities far less than c_T were measured. In this case relaxation effects due to fracture dominate over those induced by discretisation and anisotropy, keeping crack velocities in a realistic range.

4.2 Fragmentation by the branching-merging process

In the branching-merging process, contrary to a hierarchical process, fragmentation proceeds from small towards large fragments. In other words FSD evolves in time so

that the size of the largest fragment, s_0, in the distribution grows with time. FSD's of power-law form have been found experimentally for several decades, see *e.g.* [8, 18, 9, 10, 57]. There is also an abundance of simulations and conceptual models that produce power-law distributions. Both the hierarchical and the branching-merging scheme can produce an FSD of pure power-law form. The motivation for proposing the branching-merging process came from simulations: Propagating cracks were seen to generate side branches. Fragments were seen to form so that small fragments resided close to the first nucleated *main cracks* ([58, 59] and Section 4.3). To combine the experimentally observed power-laws and the spatial distributions of fragments observed in simulations into one scenario, a heuristic analytical model was presented in Publications II and III. In experimentally obtained FSD's a cut-off in the power-law form was observed in the large size regime. As will be seen, also this is naturally incorporated in the scenario, which consists of two individual processes.

In a brittle material in which material strength/stiffness variations are uncorrelated, the cracks will be nucleated in uncorrelated positions under a (spatially) homogeneous strain field. This was qualitatively confirmed from snapshots, see Fig. 1 in Publication II. As these cracks propagate, they will eventually merge, that is, a crack tip will meet and terminate at the free surface created by another crack. The FSD resulting from merging of uncorrelated cracks, which can be considered as a two-dimensional Poisson process, was shown by Grady and Kipp [55] to be of linear exponential form, see discussion in connection with Eq. (2.23).

The typical fragment size resulting from this kind of a Poisson process can be written as $s_0 \propto \rho^{-1}$, where ρ is the density of the nucleated cracks. As the cracks propagate, they generate side branches, given that the crack velocity is high enough (see Section 2.4). Main cracks thus serve as starting points for the branching-merging process we describe below.

As the elastic energy loaded in the sample by the time nucleation of cracks begins is typically high in comparison with the energy released in the formation of a fracture surface, the nucleated cracks will propagate very fast and be unstable against branching or bifurcation (or crack-tip splitting) [30]. All propagating cracks, which at the first stage are the main cracks, will thus emit side branches. The propagating side branches naturally leave two free surfaces, which attract crack tips of the neighbouring side branches. Thus adjacent side branches will attract each others. A single merging of two side branches leaves only one propagating branch: One of them terminates at the free surface created by the other, and a small-size fragment will be formed [11, 59]. The fragments formed by the first mergings taking place between branches, whose average mutual distance is l_b, are called the first-generation fragments, and the participating branches the first-generation branches. So, in an idealised scheme half of the first-generation branches will propagate further to take part in second-generation mergings. In this way the number of branches is

halved in each generation. The average distance between neighbouring branches, on the other hand, doubles when going to the next generation.

Let us denote the first generation as $i = 1$. If an initial number n_b of branches are generated from a main crack, the number of fragments n in generation i is given as $n_b/(2^{i(D-1)})$. The linear size of the fragments in generation i is $2^i l_b$, so the fragment size s in generation i is $2^{iD} s_{(i=1)}$, where $s_{(i=1)}$ is the size of the fragments belonging to the first generation. Simply by writing down the number of fragments as a function of fragment size in generation i, one gets a discrete FSD. Taking the continuum limit gives for the number density of fragments in an interval ds

$$n(s) \propto s^{-(2D-1)/D}. \tag{4.1}$$

The description given above is of course for an idealised scheme, but it can be generalised with plausible additional assumptions to a distribution for branch-to-branch distances and to a case when only a certain portion of the side branches participate in the process.

In the mining engineering literature the experimentally observed Gaudin- Schuhmann (GS) distribution for the cumulative mass of fragments of linear dimension less than r is given as $M(r) \propto r^\gamma$, where $\gamma \approx 1$. The distribution of the form in Eq. (4.1) is seen to conform with the GS distribution as $r^D \propto s$. Thus, $M(r) = \int_0^r n(r')dr' \propto \int_0^r (r')^D (r')^{-(2D-1)} (r')^{D-1} dr' \propto r$.

In simulations the branching-merging process was seen to propagate a finite distance away from the first formed main cracks. This is due to relaxation and dissipation taking place in the material. Randomly distributed broken beams naturally relax the strained lattice just as cracks nucleated from them. A propagating crack also dissipates energy. These effects cause the side branches eventually to get arrested. In FSD the finite propagation distance of side branches shows as a cut-off at large fragment sizes, consistently with experimental observations. This crack arrest is taken into account by introducing a *penetration depth* parameter λ, which is an average measure of the finite distance to which the branching-merging process proceeds.

The branching-merging process effectively takes up space/mass from the fragments generated by the Poisson process. Thus, assuming the large-size cut-off in FSD to be of exponential form, a reduced linear size can be defined for the Poisson-process fragments as $l^* = s^{\frac{1}{D}} + \lambda$. The cut-off is thus incorporated in FSD by a term of the form $\sim \exp\left(\frac{-(l^*)^D}{s_0}\right)$. The propagation (or penetration into the Poisson-process fragments) of the branching-merging process is taken into account in FSD by a term of the form $\sim s^{-\alpha} f_1(s/s_1)$, where $\alpha = (2D-1)/D$ is the power-law exponent of Eq. (4.1). f_1 is a scaling function that produces the cut-off with s_1 the effective cut-off size. It must be proportional to the penetration depth such that $s_1 \sim \lambda^D$.

Assuming, for simplicity, an exponential form for the scaling function, FSD can thus be written in the form

$$
\begin{aligned}
n(s) \quad \propto \quad & (1 - \beta_r)s^{-\alpha} \exp\left(\frac{-2^D s}{\lambda^D}\right) + \\
& \beta_r \exp\left(\frac{-(l^*)^D}{s_0}\right),
\end{aligned}
\tag{4.2}
$$

where 2^D is a mere geometric factor, and β_r determines the relative normalisation of the two parts of the distribution.

4.2.1   Simulations and experiments I

In order to check the validity of the FSD of Eq. (4.1) in 2D, simulations were performed for the minimal lattice model of Section 3.2.1 with two types of disorder. The lattice sites were slightly randomly distorted from their regular positions. The amount of distortion was controlled with parameter δ_1 which can take values between 0 and 1, where 0 corresponds to zero distortion and 1 to a chosen maximum (small) distortion. In order to mimic disorder commonly present in brittle materials, uniformly distributed uncorrelated variations in the Young's modulus E of the beams ($E \in [1 - \delta_2, 1 + \delta_2]$) was used in addition, and a small fraction (δ_3) of prebroken bonds was introduced to model microcracks. The two cases studied are: (I) $\delta_1 = 0.7$, $\delta_2 = 0.0$, $\delta_3 = 0.0$, and (II) $\delta_1 = 0.3$, $\delta_2 = 0.1$, $\delta_3 = 0.001$.

It is worth while to first check the consistency of the model in the limit of large viscous damping (coefficient c), where analogy drawn from an overdamped oscillator suggests that the ratio of the penetration depth λ to the largest fragment size s_0 should decrease exponentially with increasing damping. We indeed found (Publication II) that in this limit $\lambda/s_0 = \exp(-c/\text{const})$, $c.f.$ Fig. 4.2. For the real brittle material, considered in that work, damping is small and λ correspondingly very large. We can thus safely set $\lambda = s^{1/D}$, which is the largest value for λ in practice and also reduces the number of independent parameters used for fitting the simulation and experimental results.

The model FSD, Eq. (4.2), was also compared with the results of a series of experiments (Publication II) in which 22 identical gypsum discs were fragmented by dropping them from a varying height. The discs were dropped from the heights $h = 0.25, 0.5, 0.75, 1, 1.5, 2, 2.5, 3, 3.5, 7$, and 10 m, two experiments per each height. After each impact the masses of the fragments were carefully weighed. The impact energy was sufficient to fragment the discs at the minimum height of 0.75 m. The measured cumulated FSD's for heights $h = 0.75, 3.0, 7.0$, and 10.0 m are given in Fig. 4.3. Comparison with the integrated FSD, $N(s) = \int_s^\infty n(s)ds$ with the $n(s)$ of Eq. (4.2) (solid line), is made.
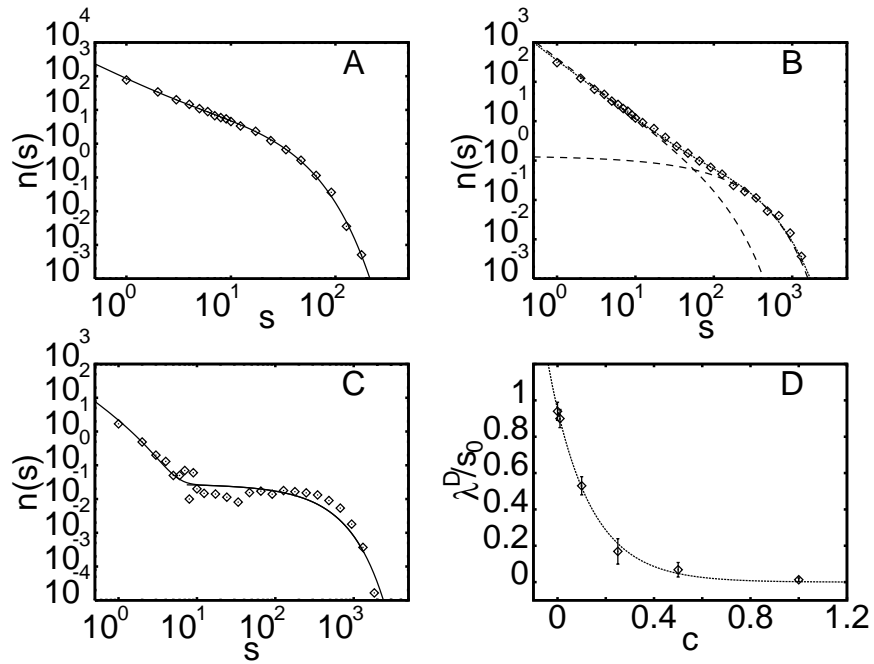
Figure 4.2: $n(s)$ for disorder type I with (**A**) Breaking threshold of a beam $\epsilon_c = 0.018$ and (**B**) $\epsilon_c = 0.025$. The numerical distributions are fitted by Eq. (4.2). In (**A**) $s_0 = 32.5$ and in (**B**) $s_0 = 460$. The number of free parameters is reduced by using $\lambda^D = s_0$. The two terms of Eq. (4.2) are also shown separately in (**B**). (**C**) is the same case as in (**A**) but with a large damping coefficient $c = 1.0$. In this case $s_0 = 430$ and $\lambda = 4.0$. (**D**) shows λ^D/s_0 as a function of c. Simulation data are compared to the exponential function $\lambda^D/s_0 = exp(-c/\text{const})$.
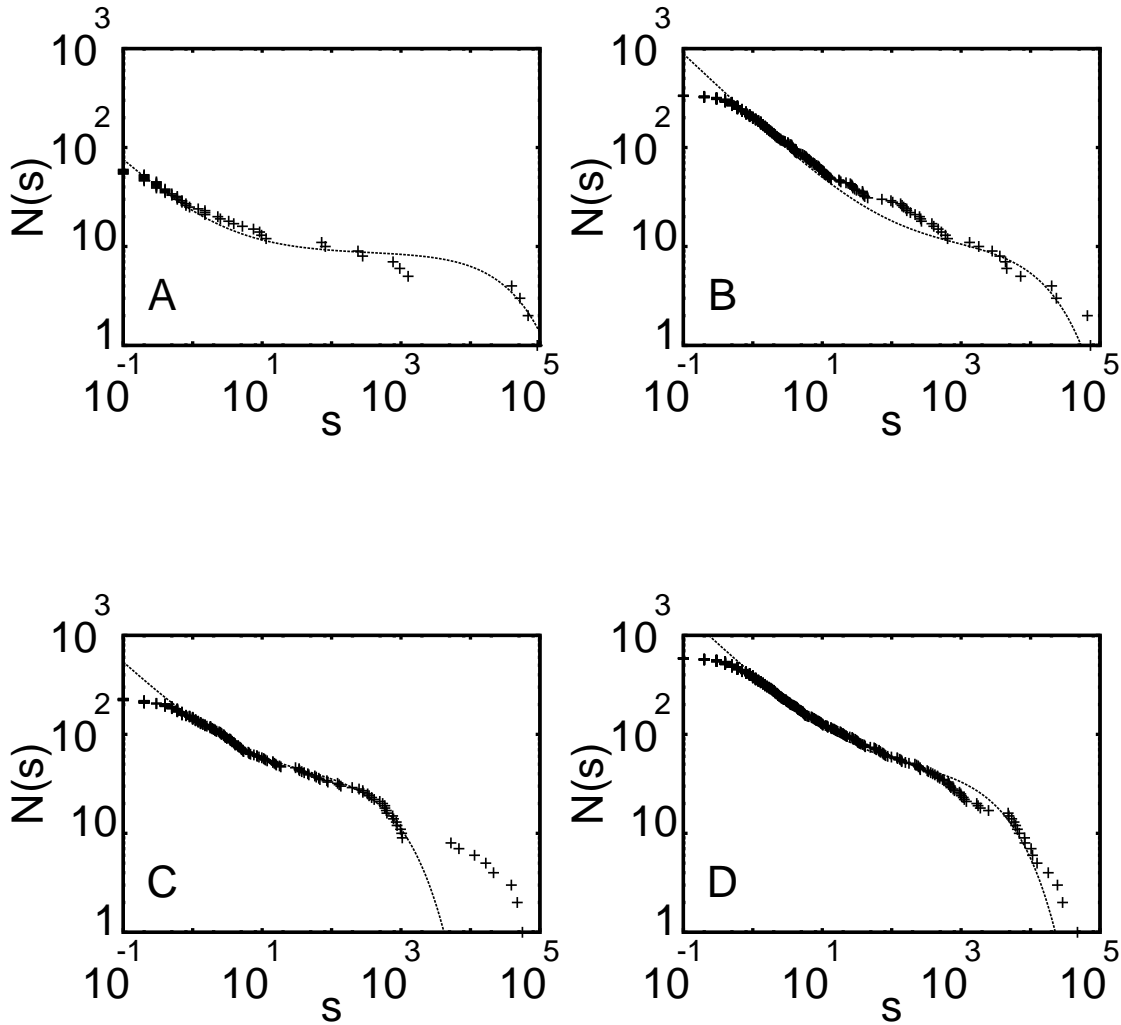
Figure 4.3: Fragment-mass distributions $N(s, \lambda, \beta_r)$ obtained for different dropping heights h. In (**A**) $h = 0.75$ m, and function $10N(s, 75, 1.3 \times 10^{-4})$ is shown as a line. In (**B**) $h = 3.0$ m and the line is $130N(s, 55, 3 \times 10^{-5})$, in (**C**) $h = 7.0$ m and the line is $75N(s, 19, 5 \times 10^{-3})$, while in (**D**) $h = 10.0$ m and the line is $250N(s, 33, 3.2 \times 10^{-4})$. From Fig. (**C**) it appears that only one part of the disc has fragmented properly. The rest of it has probably been cleaved into a few large fragments.
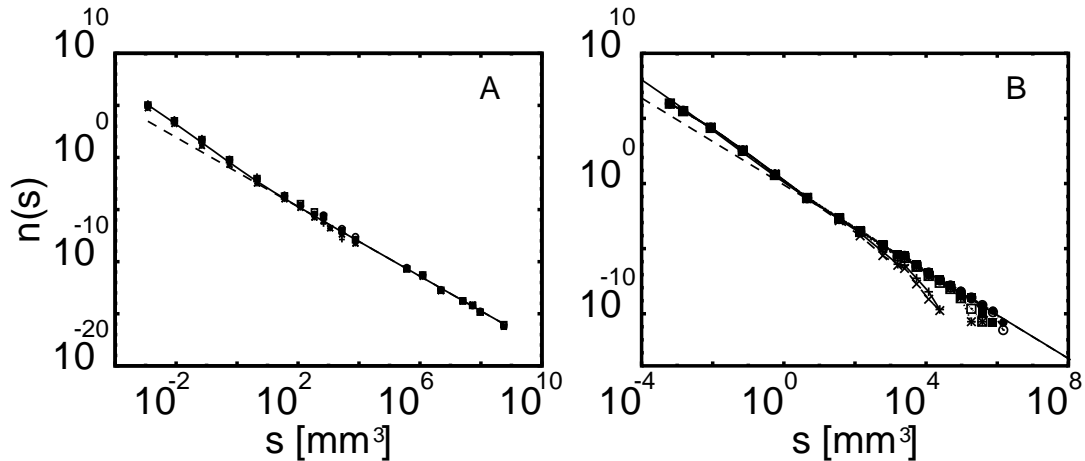
Figure 4.4: (**A**) Experimental fragment-size distributions from quarry blastings and (**B**)laboratory experiments on cylinders. The quarry data are fitted by $n(s)$ of Eq. (4.1) (broken line), and by $\hat{n}(s)$ (full line), corresponding to $\lambda \rightarrow \infty$, and $b = 14.0$. The laboratory data are fitted likewise, except that $b = 2.6$.

Obviously, the statistics of the experiments is quite limited inducing large variations to the data. The fit to Eq. (4.2) is decent for about one third of the experiments. For smaller impact energies (*i.e.* heights) the data could be better fit using exponents smaller than the one predicted by the branching-merging process. We will return to this point in Section 4.3.

4.2.2 Experiments II

The large-scale blastings of granite gneiss in the Bårarp quarry in Sweden provide Publication III [60] with a far better statistics for proper comparison with the model FSD of Eq. (4.2) than the gypsum disc experiments above. Seven single-row rounds were blasted in a $10-12$ m long and 5 m high bench, with different hole sizes but with a roughly constant specific explosive charge, $q \approx 0.55$ kg/m³. A multi-step weighing process gave 19 size fractions from $0-0.075$ mm to 500+ mm, plus boulders which were counted and weighed separately. This resulted in an FSD covering almost four orders of magnitude in linear size, or 12 orders of magnitude in mass. The obtained FSD is shown in Fig. 4.4A.

Additionally, seven cylindrical rock samples were cut from Bårarp rock and blasted in a closed blasting chamber [61]. The sample diameters chosen were $100, 200, 250,$ and 300 mm, and the specimens' height-to-diameter ratios were in the range $1.2 - 2.1$. A single central hole was drilled. The specific charge was in the range $0.36 - 2.9$ kg/m³. The complete sieving process gave 20 size fractions ranging from $0 - 0.063$ mm to 100+ mm, covering more than three orders of magnitude in
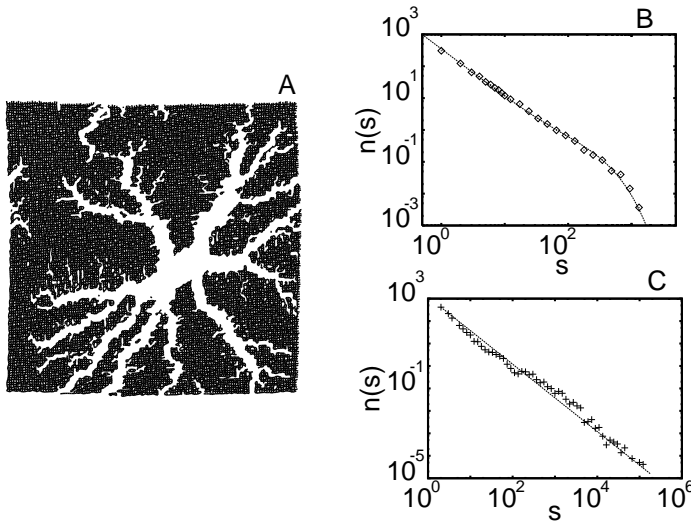
Figure 4.5: (**A**) Snapshot fom a simulation of a small brittle membrane at an early stage of fragmentation (broken bonds are removed so they appear white). (**B**) The final fragment-size distribution averaged over ~ 30 simulated configurations for $\epsilon = 1.2$. The curve is a fit to the data by Eq. (4.2). (**C**) Fragment-size distribution from simulations using minimal external strain ($\epsilon = 1.0$) required for fragmentation. The line is a fit by Eq. (4.1).

linear size. These data are given in Fig. 4.4B.

Because the power-law contributions were now very pronounced in the resulting FSD's, the data from these measurements were fitted with the scale-invariant pure power-law form Eq. (4.1). In granular rock the grains are much harder than grain boundaries such that fracture mostly takes place along these boundaries. One therefore gets in the small fragment size limit a noticeable contribution from grains which typically have a log-normal size distribution. We can take this effect into account by introducing a log-normal 'correction' in the size distribution,

$$\hat{n}(s) = n(s)[1 + bg_r(s)]ds, \tag{4.3}$$

where b is the 'strength' of the correction. Here $g_r(l) \propto \exp[-(\phi(l) - \epsilon)^2/w]$, with $\epsilon \approx -3$ and $w \approx 10$, and $\phi(l) = -\log(l)$ is the grain-size parameter used in the so-called Udden-Wentworth scale. The typical grain-size for this type of rock ranges from 3 to 10 mm.

As is evident from Fig. 4.4, the fit of the large-scale experimental data by Eq.(4.1), and especially by its corrected form $\hat{n}$ Eq.(4.3), is excellent in the infinite penetration depth limit valid for crystalline rock exhibiting negligible damping for crack propagation. Fig. 4.5 shows FSD's obtained from the simulations that used the minimal model and the model where scaling dynamics is incorporated together with a snapshot from a minimal model simulation.

4.2.3 Correlation length

In the small damping limit considered here, $s_0^{1/D}$ can be considered as a correlation length, *i.e.* the typical maximum distance between beams belonging to the same fragment. Close to the transition point in strain, ϵ_b, between the damaged and fragmented states, which appears at strain $\epsilon = \epsilon_b$, the scaling of s_0 can be investigated through the probability $\Pi(\epsilon, L_s)$ of a system of size L_s fracturing at threshold ϵ. By defining probabilities shifted with respect to the transition point ϵ_b such that $\hat{\Pi}(\epsilon_s, L_s) = \Pi(\epsilon - \epsilon_b(L_s), L_s)$, where $\hat{\Pi}(0, L_s) = 0.5$, a data collapse in the form $\hat{\Pi}((\epsilon - \epsilon_b(L_s)L_s^{1/\nu}, L_s)$ with ν the correlation length exponent, was performed along with a fit of $\Pi(\epsilon, L_s)$ by a Gaussian curve (Publication II). In the Gaussian fit the standard deviation should scale as $L_s^{-1/\nu}$. The correlation length $s_0^{1/D}$ appeared to diverge according to a power law at the transition point. Both fits gave the correlation exponent $\nu = 4 \pm 1.0$, which differs from that reported in [17]. By fitting $\sqrt{E} - \sqrt{E_c}$ obtained from the experimental data as a function of $s_0^{1/D}$, we obtained $\nu \approx 0.25$ and $\nu \approx 1.1$ for the correlation length exponent in Publications II and III. (In Publication III there is a misprint: The fit has been performed using $(1/\gamma_v)^{1/3}$ and not $1/\sqrt{\gamma_v}$ as indicated in Fig. 3). We can thus infer that the correlation length exponent ν is not universal for brittle fragmentation, but apparently depends on loading conditions. A minor difference in ν was also found between the two types of disorder investigated (see Section 3.2.1).

We can thus conclude that the conceptual model for fragmentation by a combination of a Poisson process and a scale invariant branching-merging process explained satisfactorily the experiments reported in Publication II and excellently the ones in Publication III. Different correlation length exponents ν were found for the experiments and for the simulations. This is quite natural as there seems to be no reason to expect universality in the correlation length, which is rather a system and loading dependent quantity.

4.3 Dimensional effects in fragmentation

The numerical model introduced in Section 3.2.2 describes a fully periodic two-dimensional brittle system, *i.e.* a torus, embedded in a three-dimensional space. In this way we can analyse dimensional effects in dynamic fragmentation, that is whether fragmentation is in this case different from the process described in the previous section, in which fragmentation of D-dimensional systems was considered in D-dimensional space for $D = 2$ and $D = 3$. To begin with we show that the former process is reduced to the latter if we freeze out the out-of-plane motion in the former case. This freezing out can easily be made by increasing the inertia

in the radial direction of the system. In the large inertia limit we applied on a perfectly ordered beam lattice a constant force loading, *i.e* $F_i^e(t) = \text{const} \neq 0, \forall i$, in Eq. (3.10). In this way we were able to produce the power-law form $n(s) \sim s^{-1.5}$, for the number density of fragments and at the same time see that essentially all cracks started from an initially broken beam. An advantage of this force-loading scheme is that the spatial development of fragmentation can relatively clearly be discerned. Cracks were seen to propagate, branch, and merge in directions away from the first-formed main cracks and finally stop due to dissipation and relaxation. This finite propagation could thus be depicted by a *penetration depth* λ, as described in Section 4.2. We can thus conclude that the two realisations of our numerical model give the same results under similar conditions.

We now proceed to consider fragmentation of the two-dimensional surface of the torus in a three-dimensional space such that the out-of-plane motions of the surface are not frozen out (Publication IV). A motivation to this problem is provided by earlier results by Oddershede *et al.* [9]. They observed the exponent of the power-law FSD vary with an effective dimension of the objects (varying between two and three) broken in our familiar three-dimensional space. So far these results have remained unexplained.

The system was loaded initially such that an impulse corresponding to homogeneous expansion was given in the direction of the radius of curvature. The system thus resembles an inflated closed brittle surface in free space, which undergoes Newtonian dynamics. When the deformation of a beam exceeded a given breaking threshold, it was simply removed. In order to describe a real disordered material with defects, we also introduced initially a number of uncorrelated defects in the form of individual removed beams.

The time evolution of the fragmentation process showed clearly that while fragment formation started with small fragments close to the first propagating cracks and proceeded towards larger ones farther away, some large fragments divided further into smaller fragments. Thus, the fragmentation process is now clearly comprised of two parts: a branching-merging process proceeding from small towards large fragments, and some kind of hierarchical process proceeding in the opposite direction. Before going into a more detailed description of this complicated fragmentation process, we introduce briefly a simple model for hierarchical fragmentation as it will help us in the analysis of simulation results.

We choose the model of Kadono and Arakawa [12] to represent a hierarchical fragmentation process because it is so simple but captures however some of its essential features. From Eq. (2.36), using $s_i = r_i^{1/2}$, we find $N(> s_i) \sim s_i^{-(1+\ln p/\ln b^2)}$, when denoting the fragment generation by i. Thus,

$$n(s) \sim s^{-(2+\ln p/\ln b^2)}. \tag{4.4}$$

The average size or mass in generation i can be written as

$$
\begin{aligned}
\bar{s}_i &= \frac{(1-p)b^2(1/b)^2 + (pb^2)(1-b)b^2(1/b)^4 + \ldots + (pb^2)^{i-1}(1-p)b^2(1/b)^{i+1}}{(1-p)b^2 + (pb^2)(1-p)b^2 + \ldots + (pb^2)^{i-1}(1-p)b^2} \\
&= \frac{(1/b)^2[1 + (pb^2)(1/b)^2 + \ldots + (pb^2)^{i-1}(1/b)^{2(i-1)}]}{1 + (pb^2) + \ldots + (pb^2)^{i-1}} \\
&= \frac{(1/b)^2 \sum_{i'=0}^{i-1} p^{i'}}{\sum_{i'=0}^{i-1}(pb^2)^{i'}}.
\end{aligned}
\tag{4.5}
$$

The ratio of average masses in consequent generations is hence given by

$$
\bar{s}_{i+1}/\bar{s}_i = [1 + (pb^2)^n / \sum_{i'=0}^{i-1}(pb^2)^{i'}]^{-1}
$$

$$
\lim_{i\to\infty} \bar{s}_{i+1}/\bar{s}_i = 1/(pb^2).
\tag{4.6}
$$

On the other hand, the average mass of the branching-merging process (with the residual included) can be written as

$$
\bar{s}_i = \frac{S}{1 + N_I \sum_{i'=0}^{i} h^{-i'}} \sim \frac{1}{1 - h^{-i}},
\tag{4.7}
$$

where S is the total system mass, and N_I is the number of fragments in the first generation of the process.

If we now follow in the simulations the evolution of the fragmentation process, the fragments were seen to be distributed in two distinct parts, a small-size part, extending with time towards increasing fragment sizes, and a large-fragment or residual part. The averaged maximum size of the small-fragment part, $s_{max}^{<}$, was seen to grow as $\sim \exp(\text{const } n_{br})$, where n_{br} is the number of broken beams - linearly dependent upon i in accord with the branching-merging process, *c.f.* Fig. 4.6A. The branching-merging process stops as $s_{max}^{<}$ reaches the average size of all fragments. This is explained by the fact that side branches cannot propagate farther than the average distance between the main cracks. Up to this point the overall maximum fragment size s_{max} stays rather constant, followed by crossover to a power-law decay. This behaviour of s_{max} illustrates the fact that fragmentation does not now stop when the branching-merging process stops, unlike in the case of the minimal model. It proceeds by a hierarchical fragmentation process whereby large fragments already formed during the first phase (dominated by the branching-merging process), are broken further. This is also demonstrated by the FSD's shown in Fig. 4.6B. The exponent α, initially 1.5 in agreement with the branching-merging process, begins to decrease when $s_{max}^{<}$ reaches the average fragment size, levelling off at a final value of ≈ 1.2, *c.f.* Figs. 4.6B and 4.7B.
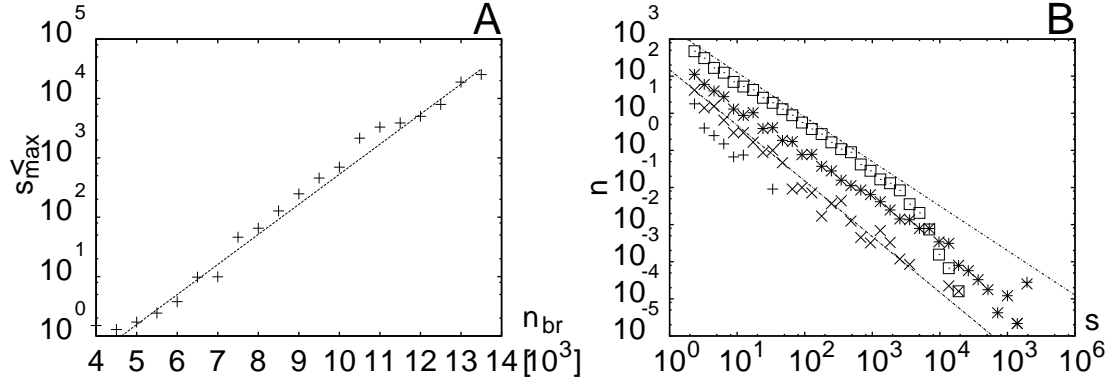
Figure 4.6: (**A**) Average $s_{max}^<$ as a function of the number of broken beams n_{br}. The line fitted to the data is $\sim \exp(1.17 \cdot 10^{-3} n_{br})$. (**B**) The evolution of the simulated fragment-size distribution when time is measured with the number of broken beams: (+) $n_{br} = 7000$, (×) $n_{br} = 11000$, (∗) $n_{br} = 15000$, (⊡) $n_{br} = 27000$. Lines $\sim s^{-1.5}$ and $\sim s^{-1.2}$ are also shown as guides for the eye.
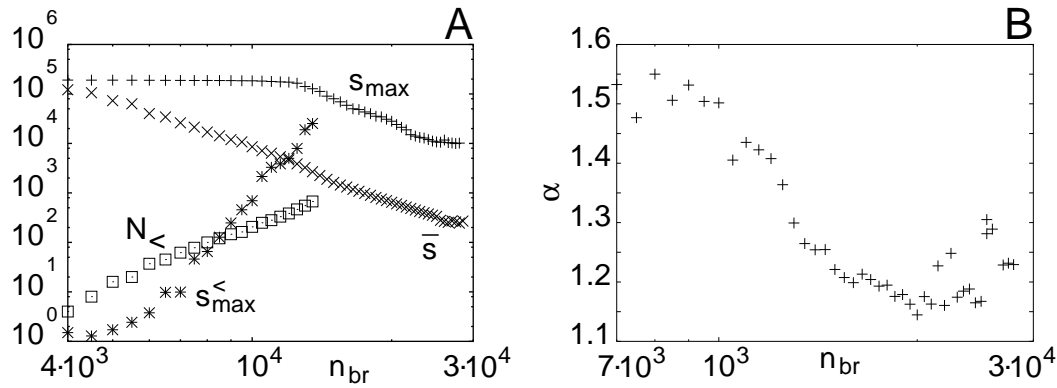

Figure 4.7: Simulated development of the fragment-size distribution as a function of n_{br}. (**A**) (+) Average maximum fragment size s_{max}, (×) average fragment size $\bar{s}$, (∗) average maximum fragment size of the small-size part of the distribution $s_{max}^<$, and (⊡) number of fragments in the small-size part $N_<$. (**B**) The scaling exponent α as obtained from fitting the number density of fragments by $n(s) \sim s^{-\alpha}$, as a function of n_{br}.
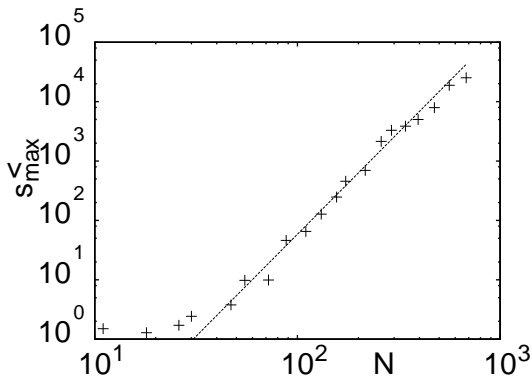
Figure 4.8: $s_{max}^<$ as a function of the number of fragments N. A power-law fit gives $s_{max}^< \sim N^{3.44}$, which is shown as a line.

From Fig. 4.7 the average fragment size $\bar{s}$ is seen to decrease with increasing n_{br} according to a power-law. According to Eq. (4.7), for the branching-merging process $\bar{s}$ should after an initial decrease level off at a constant value. Thus the behaviour of $\bar{s}$ should essentially be determined by the hierarchical process. From Eq. (4.6) we can deduce that for a hierarchical process $\bar{s}$ decreases exponentially as a function of i. By inspection it can be seen that for p sufficiently large $i \sim \exp(\text{const } n_{br})$ in this process. Combining the two relations gives a power-law decrease of $\bar{s}$ as a function of n_{br} in accord with Fig. 4.7A.

The relevant time scales related to the branching-merging and hierarchical processes are very different. The branching-merging process is initially very fast in producing the small-size part of FSD, so that the largest fragment of this part grows, as explained above, exponentially with n_{br}. The hierarchical process takes off very slowly, but eventually begins to form new fragments at a rate which grows exponentially with n_{br}, while not appreciably affecting the growth of $s_{max}^<$ that is still dominated by the branching-merging process. By that time the latter process produces new fragments with a rapidly decreasing growth rate. There should thus be an interval in the fragmentation process during which $s_{max}^< \sim N^\beta$ with β a constant. Here as before N is the total number of fragments (which depends on time). We show in Fig. 4.8 a simulated $s_{max}^<$ as a function of N. These data display a clear power-law dependence with $\beta \approx 3.44$.

The secondary cracks that are responsible for the hierarchical fragmentation process were observed to be spatially correlated: new cracks had a tendency to form preferrably near already existing cracks. Their distribution is thus not Poissonian in contrast to that of the main cracks which appear in fragmentation in a two-dimensional space, *c.f.* Fig. 4.11.

As there is now a nonzero radius of curvature, relaxation of strain at the (1D) crack surfaces in enhanced, which induces strain peaks in the vicinity of them. The
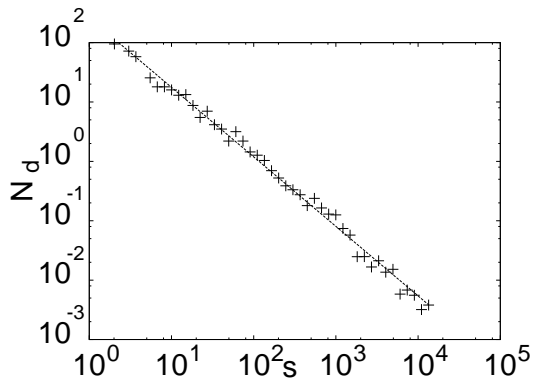
Figure 4.9: Differential FSD's $N_d(n_{br} = 17000)$. The fitted line is $N_d \sim s^{-1.17}$.

extra dimension allows thereby stress enhancement close to existing cracks such that the fracture threshold is there more easily exceeded.

As there is a power-law contribution to FSD even after the operation of the hierarchical process, albeit with a changed scaling exponent, it is evident that the correlated nature of the secondary cracks renders the process scale invariant. In order to find the related scaling exponent, we plotted the differential fragment-size distribution $N_d(n_{br}) \equiv N(n_{br}) - N(n_{br}^{(o)} = 11500)$ for $n_{br} > 11500$. This differential distribution is dominated by the hierarchical process as $n_{br}^{(o)} = 11500$ marks the crossover in the relative dominance of the two processes. We show the differential distribution in Fig. 4.9 for $n_{br} = 17000$. It is evident that the process is indeed scale invariant with a scaling exponent of ~ 1.17. A large-size cutoff begins to appear at $n_{br} = 18500$.

The effect of the hierarchical process was also confirmed by simulating a system in which side-branch formation was inhibited after an unlimited formation of the first 1000 broken beams. Already at $n_{br} = 5000$ the resulting FSD had acquired a power-law form with the exponent $\alpha \approx 1.25$ in the whole size range. Snapshots of this process are shown in Fig. 4.10. Comparing these to the snapshots of fragmentation with an initial Poisson distribution of defects, Fig. 4.11, the hierarchical process is seen to be more pronounced now when branching is inhibited, as expected.

In the fragmentation process where there were no broken beams initially in the beam lattice, the previously extracted features were seen to be present. The cut-off at large fragment sizes, $c.f.$ Fig. 4.12B, is now stronger than in the case with an initial Poissonian distribution of defects [13, 4]. Again, from the growth of $s_{max}^{<}$ as a function of n_{br}, $c.f.$ Fig. 4.12A, it can be inferred that the small-size part of FSD is formed by the branching-merging process.

We can thus conclude that fragmentation of a two-dimensional toroidal surface is a process which begins with nucleation of main cracks followed by a merging process at their side branches. Thereafter nucleation of secondary cracks takes
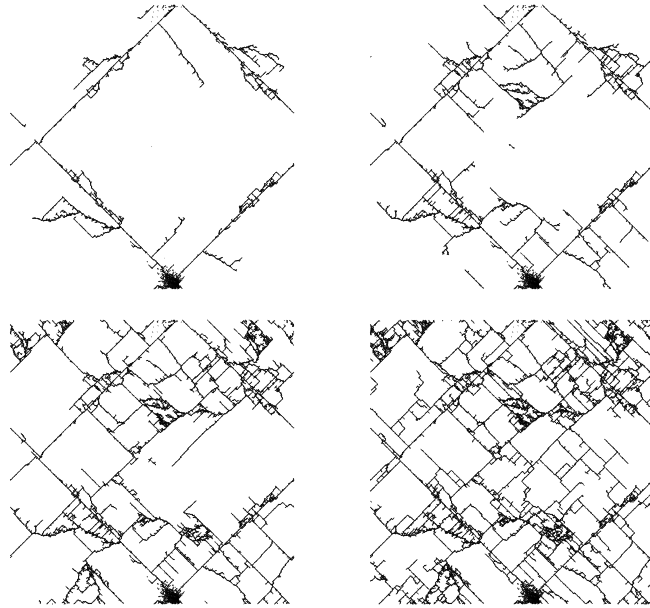
Figure 4.10: Snapshots of a disordered lattice undergoing fragmentation in which formation of branches is inhibited. (**A**) $n_{br} = 6000$, (**B**) $n_{br} = 12500$, (**C**) $n_{br} = 14500$, (**D**) $n_{br} = 27000$
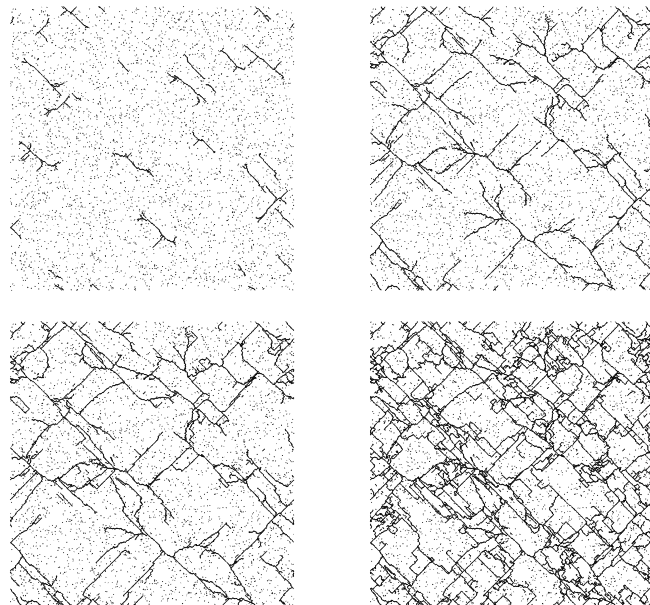

Figure 4.11: Snapshots of a disordered lattice with defects undergoing a fragmentation: (**A**) $n_{br} = 6000$, (**B**) $n_{br} = 12500$, (**C**) $n_{br} = 14500$, (**D**) $n_{br} = 27000$.
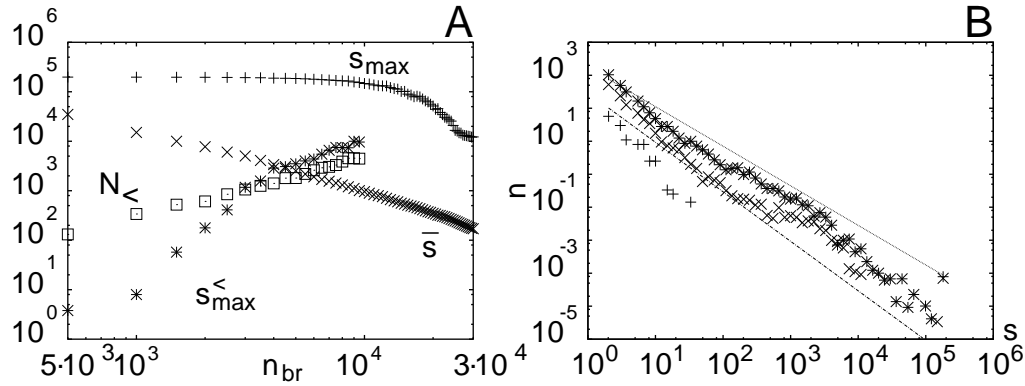
Figure 4.12: Fragmentation with no initial defects. (**A**) Curves marked as in Fig. 4.7(**A**). (**B**) Evolution of FSD's (+) $n_{br} = 1000$, ($\times$) $n_{br} = 6500$, ($*$) $n_{br} = 19000$. Lines $\sim s^{-1.5}$ and $\sim s^{-1.2}$ are shown to guide the eye.

effect. Because of relative strong elastic relaxation at the crack surfaces, these secondary cracks are spatially correlated: they are preferably formed in the vicinity of the already existing cracks. Merging of these secondary cracks with existing cracks creates a hierarchical fragmentation process whereby existing (or forming) fragments are broken further. The branching-merging process determines, through growth of $s_{max}^<$, the size range on which the hierarchical process operates. At later stages, as the branching-merging process is restricted by the average distance of the main cracks, the hierarchical process dominates fragmentation and produces an FSD of the form $\sim s^{-1.2}$.

The fragmentation mechanisms described above explain well the dimensional dependence of the power-law exponents in the FSD's of the experiments by Oddershede *et al.* [9]. The measured values of ≈ 1.2 and ≈ 1.55 for α in 2D and 3D objects, respectively, closely coincide with the values obtained in the simulations for the two versions of our numerical model, applicable in the respective cases (see Table 2.2). We can now also explain to the deviation of the experimental data from the result of the branching-merging model in Publication II. As already mentioned in the beginning of the section, in the limit of high inertia in the radial direction, which corresponds to approaching the situation in which a 2D object is fragmented in a 2D space, the exponent 1.5 was again obtained for the power-law FSD. When moving away from this limit towards the state in which dynamics take place in three dimensions, or a 2D object fragments in 3D, the power-law exponent 1.2 results. Thus, the *the effective spatial dimensions available for dynamical fragmentation* seem to determine, which of the possible processes take part in the overall fragmentation.

Chapter 5

Conclusion

With the aid of two numerical models we have investigated the fragmentation process that takes place in a two-dimensional disordered brittle medium embedded in two- or three-dimensional space. The static as well as dynamical applicability of the models for simulation of brittle fragmentation was verified by thorough benchmarking. For fragmentation in which the spatial dimension and the dimension of the fragmenting object are equal, an analytical model based on branching and merging of propagating cracks was presented. This analytical and the respective numerical model produced the available experimental fragment-size distributions (FSD) with excellent accuracy in the case of equal object and spatial dimensions. The exponent of the power-law part of FSD was determined to be $(2D-1)/D$ with D the spatial dimension. Nucleation of cracks was found to occur randomly without any correlation induced by loading. Both the power-law and the exponential part of FSD could be explained by the model. The nature of this dynamic process was confirmed by time-dependent simulations and analysis.

In the numerical model in which a two-dimensional brittle disordered medium fragments in a three-dimensional space, FSD was found to acquire a form different from that produced in two-dimensional space. Fragmentation was found to be comprised of a branching-merging process as in the previous case, but also of an additional hierarchical process. The hierarchical part was found to dominate in the regime where the largest fragments produced by the branching-merging process are of the same order of magnitude as the average fragment size, i.e. when the side branches around the main cracks have reached the average distance between them. The hierarchical process is facilitated by the presence of the extra spatial dimension which allows out-of-plane motion so that larger fragments are in this case more unstable against further fragmentation. An exponent of ≈ 1.2 was obtained for the power-law FSD produced by a combined process in which the hierarchical part was significant. The extra spatial dimension was found to induce spatial correlation

45

in the nucleation of cracks so that the hierarchical process produces also in itself a scale-invariant FSD. The scaling exponent of the hierarchical process alone was found to be 1.17.

Our results provide an explanation to the results of previous fragmentation experiments in which the effective dimension of the fragmented objects had varied between two and three. In addition there are very recent results on fragmentation of egg shells [62, 63], which appear to be understandable in terms of the fragmentation mechanisms described above. The stiffness of the shells used in combination with the way the energy is imparted in loading may be factors that determine in this case the loading-dependent significance of hierarchical fragmentation, i.e. the observed exponent of the power-law FSD. This problem needs, however, a more detailed analysis.

The introduced modes will no doubt prove helpful in future experimental and theoretical work concerning fragmentation. Identification of the participating processes also provides means for analysing fragmentation using alternative approaches. A master equation analysis could in this respect prove very useful. Information obtained from the simulations enables one to write down the dynamical probabilistic equations governing the developing fragment-mass distribution. Investigation of the behaviour of these equations could benefit from analogies to other more extensively studied dynamical non-equilibrium systems and the results already obtained for them.

Bibliography

[1] *Statistical Models for the Fracture of Disordered Media*, edited by H.J. Herrmann and S. Roux (North-Holland, Amsterdam, 1990).

[2] *Fragmentation Phenomena*, edited by D. Beysens, X. Campi, and E. Pefferkorn (World Scientific, Singapore, 1995).

[3] R.M. Ziff and E.D. McGrady, Macromolecules **55**, 2513 (1986).

[4] J.A. Åström, F. Ouchterlony, R.P. Linna, J. Timonen, Phys. Rev. Lett. **92**, 245506 (2004).

[5] C.J. Cunningham, *Introduction to Asteroids* (Willmann-Bell, Inc., Richmond, VA, 1988).

[6] S. Redner in *Statistical Models for the Fracture of Disordered Media*, edited by H.J. Herrmann and S. Roux (North-Holland, Amsterdam, 1990).

[7] F. Kun and H.J. Herrmann, Phys. Rev. E **59**,2623 (1999).

[8] J.J. Gilvarry and B.H. Berstrom, J. Appl. Phys. **32**, 400 (1961).

[9] L. Oddershede, P. Dimon, and J. Bohr, Phys. Rev. Lett. **71**, 3107 (1993).

[10] A. Meibom and I. Balslev, Phys. Rev. Lett. **76**, 2492 (1996).

[11] H. Inaoka, E. Toyosawa, and H. Takayasu, Phys. Rev. Lett. **78**, 3455 (1997).

[12] T. Kadono, M. Arakawa, Phys. Rev. E. **65**, 35107 (2002).

[13] J.A. Åström, R.P. Linna, J. Timonen, et al., accepted for publication in Phys. Rev. E.

[14] J.J. Gilvarry, J. Appl. Phys. **32** 391 (1961).

[15] M. Marsili and Yi-Cheng Zhang, Phys. Rev. Lett. **77**, 3577 (1996).

[16] M. Kloster, A. Hansen, and P.C. Hemmer, Phys. Rev. E **56**, 2615 (1997).

[17] J.A. Åström, B.L. Holian, J. Timonen, Phys. Rev. Lett. **84**, 3061 (2000).

[18] D.L. Turcotte, J. Geophys. Res. **91**, 1921 (1986).

[19] A.M. Gaudin and T.P. Meloy, Trans. AIME/SME **223**, 40 (1962); **223**, 43 (1962).

[20] R.R. Klimpel and G.L. Austin, Trans. AIME/SME **232**, 88 (1965).

[21] A.N. Kolmogorov, *Doklady Akad. Nauk. SSSR* **31**, 99 (1941).

[22] E.C. Dapples, *Basic Geology for Science and Engineering* (Wiley, New York, 1959).

[23] *Models of Geologic Processes; An Introduction to Mathematical Geology*, edited by P. Fenner (American Geological Institute, Washington, 1969).

[24] P. Habib, *Soil and Rock Mechanics* (Cambridge University Press, Cambridge, 1983).

[25] T.H. Wu, *Soil Mechanics* (Allyn and Bacon, Boston, 1966).

[26] A.A. Griffith, Phil. Trans. Royal Soc. **A221**, 163 (1920).

[27] N.F. Mott, Engineering **165**, 16 (1948).

[28] G.R. Irwin, J. Appl. Mech. **24**, 361.

[29] L.B. Freund, *Dynamic fracture mechanics* (Cambridge University Press, Cambridge, 1998).

[30] J. Fineberg, M. Marder, Phys. Rep. **313**, 1 (1999).

[31] L.D. Landau and E.M. Lifshitz, *Theory of Elasticity* (Pergamon Press, London, 1959).

[32] V. Prakash, R.J. Clifton, in *Fracture Mechanics: 22nd Symp.*, edited by H.A. Ernst, *et al.* (**1**, American Society for Testing and Materials, Philadelphia, PA, 1992).

[33] P. Manogg, Int. J. Fract. **2**, 604 (1966).

[34] P.S. Theocaris, E.E. Gdoutos, J. Appl. Mech. **39**, 604 (1972).

[35] J.F. Kalthoff in *Static and Dynamic Photoelasticity and Caustics*, edited by A. Lagarde (Springer, Berlin, 1987).

[36] A.J. Rosakis, J. Duffy, L.B. Freund, J. Mech. Phys. Solids **32**, 443 (1984).

[37] A.S. Kobayashi in *Handbook on Experimental Mechanics*, edited by A.S. Kobayashi (Prentice-Hall, Englewood Cliffs, NJ, 1981).

[38] H. Bergkvist, Eng. Fract. Mech. **6**, 621 (1974).

[39] J. Congleton, B.K. Denton, ASTM-STP **627**, 336 (1977).

[40] B. Brickstad, F. Nilsson, Int. J. Fract. **16**, 71 (1980).

[41] J. Fineberg, S.P. Gross, M. Marder, H.L. Swinney, Phys. Rev. Lett. **67**, 457 (1991).

[42] J. Fineberg, S.P. Gross, M. Marder, H.L. Swinney, Phys. Rev. B **45**, 5146 (1992).

[43] K.S. Kim, J. Appl. Mech. **52**, 585 (1985).

[44] B.Q. Vu, V.K. Kinra, Eng. Fract. Mech. **15**, 107 (1981).

[45] P.D. Washabaugh, W.G. Knauss, Int. J. Fract. **65**, 97 (1994).

[46] K. Ravi-Chandar, Int. J. Fract. **90**, 83 (1998).

[47] K. Ravi-Chandar, W.G. Knauss, Int. J. Fract. **25**, 209 (1984).

[48] K. Ravi-Chandar, J. Mech. and Phys. of Solids **45**, 535 (1997).

[49] E. Sharon, S.P. Gross, Phys. Rev. Lett. **74**, 5146 (1995).

[50] E. Sharon, J. Fineberg, Phys. Rev. Lett. B **54**, 7128 (1997).

[51] E. Sharon, J. Fineberg, Philos. Mag. B **78**, 243 (1998).

[52] D. Hull, J. Mater. Sci. **5**, 357 (1970).

[53] C.C. Lienau, J. Franklin Inst. **221**, 485 (1936).

[54] T. Hirata, Inst. Chem. Phys. Res. Tokyo **16**, 159 (1931).

[55] D.E. Grady, M.E. Kipp, J. Appl. Phys. **58**, 1210 (1985).

[56] N.F. Mott, E.H. Linfoot, Ministry of Supply, AC 3348 (1943); N.F. Mott, Ministry of Supply, AC 3642 (1943) ; N.F. Mott, Ministry of Supply, AC 4035 (1943).

[57] H. Katsuragi, D. Sugino, and H. Honjo,Phys. Rev. E **68**, 46105 (2003).

[58] J. Åström, J. Timonen, Phys. Rev. E **55**, 4757 (1997).

[59] J.A. Åström and J. Timonen, Phys. Rev. Lett. **78**, 3677 (1997).

[60] M. Olsson, I. Bergqvist, in *Proceedings of the Discussion Meeting BK 2002*, (Swedish Rock Construction Committee, Stockholm, 2002), 33.

[61] P. Moser, A. Grasedieck, M. Olsson, F. Ouchterlony, in *Proceedings of the EFEE 2nd World Conference*, edited by R. Holmberg (Balkema (Rotterdam, 2003)), 449.

[62] F. Wittel, F. Kun, H.J. Herrmann, and B.H. Kröplin, cond-mat/0402461 (2004).

[63] F. Wittel, F. Kun, H.J. Herrmann, and B.H. Kröplin, cond-mat/0407124 (2004).